J. Fluid Mech. (1982), *vol.* 124, *pp.* 73–108
Printed in Great Britain

Three-dimensional deep-water waves. Part 1. Experimental measurement of skew and symmetric wave patterns

By MING-YANG SU

Naval Ocean Research and Development Activity,
NSTL Station, Mississippi 39529

(Received 23 September 1981 and in revised form 29 January 1982)

The three-dimensional structures of symmetric and skew wave patterns in deep water observed in a tow tank and a wide basin are described. These symmetric waves are the result of three-dimensional subharmonic bifurcation of two-dimensional wavetrains with steepness $a_0 k_0 \geqslant 0{\cdot}25$, where a_0 and k_0 are the wave amplitude and wavenumber respectively. The wave profiles, local surface slopes and amplitude spectra at various cross-sections of the crescent-shaped symmetric waves are presented and discussed.

The skew waves are another type of three-dimensional bifurcation from a uniform wavetrain, and occur most clearly when $0{\cdot}16 \gtrsim a_0 k_0 \gtrsim 0{\cdot}18$. These skew wave patterns are found to interact between two sets of themselves propagating from different directions, and to be subject to the Benjamin–Feir type modulations. The interactions cause compact three-dimensional wave packets. Agreement between experiment and theory is found for the case of symmetric wave patterns. The bifurcation of uniform Stokes waves into symmetric wave patterns provide a new physical process for directional energy spreading.

1. Introduction

Saffman & Yuen (1980) have predicted the existence of two new types of three-dimensional permanent waveforms, resulting from bifurcations of a uniform two-dimensional Stokes wave on deep water, based on an equation due to Zakharov (1968) (see Crawford, Saffman & Yuen 1980). This equation is valid for weakly nonlinear waves. The first type of bifurcation produces a steady symmetric wave pattern propagating in the same direction as the Stokes waves. A computation of the waveforms for several configurations of the symmetric wave patterns is given by Meiron, Saffman & Yuen (1982). The second type produces the steady skew wave patterns that propagate obliquely from the direction of the Stokes waves. Their theory shows further that the skew waves are stable to infinitesimal disturbances. The purpose of this paper is to present experimental evidence for the existence and structures of the bifurcated symmetric and skew wave patterns. The skew wave patterns in § 3 are found to occur when the steepness of the initial Stokes waves is $0{\cdot}16 \gtrsim a_0 k_0 \gtrsim 0{\cdot}18$, where a_0 and k_0 are respectively the wave amplitude and wavenumber of the initial Stokes waves. In addition, two groups of the skew wave patterns propagating from different directions are observed to interact and to emerge subsequently from their interaction without apparent destruction of each other, in a manner similar to the interaction

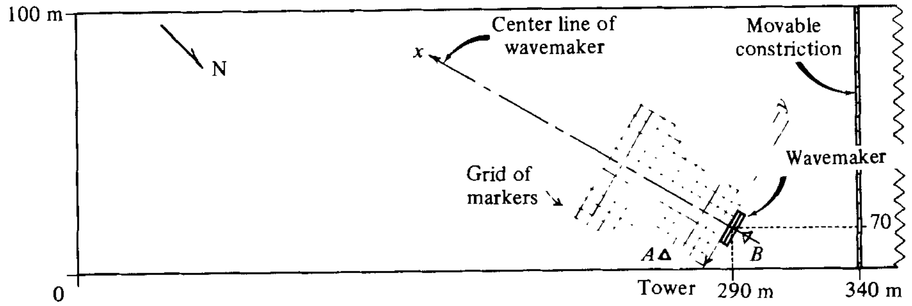

FIGURE 1. General layout of the experimental facility in the basin.

between two trains of Stokes waves. Simultaneously, in the evolution of the three-dimensional wave, subharmonic modulations (Benjamin & Feir 1967; Longuet-Higgins 1978) of the skew wave patterns are observed to form a series of compact three-dimensional wave packets on deep water.

The symmetric wave patterns in § 4 are found to be most evident when

$$0{\cdot}25 < a_0k_0 < 0{\cdot}34,$$

and are triggered by the newly discovered three-dimensional instability, which has a larger growth rate than the predominantly two-dimensional Benjamin–Feir-type instabilities for $a_0k_0 > 0{\cdot}30$ (McLean 1982; Su *et al.* 1982). Three configurations of symmetric wave patterns with different subharmonic lengths from two to four basic wavelengths have been found.

The bifurcation of uniform Stokes waves into the skew wave patterns provides a physical process for directional wave energy spreading. It has been shown by Su *et al.* (1982) that the evolution of the symmetric wave patterns also leads to directional energy spreading. Thus the Stokes-wave bifurcations may be significant factors in contributing to directional spectra of ocean waves.

The experimental method will be described in § 2, and observations and measurements in §§ 3 and 4. Interpretation and discussion of these results in the light of existing theories on the instability and bifurcation of nonlinear waves will be made in § 5.

2. Experimental method

Figure 1 shows the general layout of the experimental set-up used for skew-wave measurement located at the Naval Ocean Research and Development Activity. (The experimental set-up for symmetric wave patterns has been described in Su *et al.* (1982).) The outdoor basin is 1 m deep and 100 by 340 m wide. The normal water depth for all the experiments reported in this paper is 0·80 m above the grass bottom, which is mowed before the experiments. The plunger-type mechanical wavemaker used has a crest length of 15·9 m, a frequency range from 0·5 to 2·0 Hz, and an adjustable stroke up to 0·305 m. The front face of the plunger is hyperbolic in shape. A rectangular grid made of markers sticking out of the water surface is installed in front of the wavemaker. These markers are separated by 6·1 m in both horizontal directions, with the origin of the grid reference at the centre of the plunger. The normal to the plunger will be designated as the x-axis, and the parallel as the y-axis, with y positive toward the left.

A foldover tower of 70 ft height is located in either of the locations A or B indicated in figure 1. The tower is used for providing a vantage point for direct observations and for taking photographs and motion pictures of the evolving wave patterns. These photographs are found to be indispensable for studying the rather complex three-dimensional wave phenomena.

In situ measurements of water-surface displacement due to waves in the time domain are made by an array of capacitance-type wave gauges, with the sensing wires made of double-coated magnet wire 0·5 mm in diameter. The surface-displacement records thus obtained are first low-pass filtered with a cut-off frequency of 40 Hz, digitized at a rate of 40 samples/s, and finally stored on magnetic tapes for further analysis. The direct analogue outputs from the wave gauges are also used for producing wave profiles from a four-channel oscillograph, and for obtaining power spectra from an on-line spectrum analyser. More detailed information related to experimental facilities, instrumentation and experimental procedures are described in Su *et al.* 1982.

3. Stuctures of skew wave patterns

Since it is found that the skew wave patterns show up when $0{\cdot}16 \gtrsim a_0k_0 \gtrsim 0{\cdot}18$, we shall use a typical example with $a_0k_0 = 0{\cdot}17$ to illustrate typical characteristics of the wave patterns observed in our experiments. For clarity in presenting the rather complicated three-dimensional wave patterns, the entire wave field is divided into the following five regimes, each of which has its distinctive feature:

(i) Stokes waves,
(ii) skew wave patterns,
(iii) interactions of skew wave patterns,
(iv) Benjamin–Feir modulations of Stokes waves,
(v) Benjamin–Feir modulations of skew waves.

Locations of these five regimes are shown in figure 2 for easy reference to the later description of each regime separately. For the example with $a_0k_0 = 0{\cdot}17$, the other wave parameters used are $f_0 = 1{\cdot}24$ Hz, $a_0 = 2{\cdot}7$ cm, $\lambda_0 = 0{\cdot}95$ m and $c_0 = 1{\cdot}25$ m/s.

3.1. *Stokes waves*

The first regime is composed of uniform Stokes waves which are generated by the mechanical wavemaker. The transient characteristics associated with the particular wave-making process die out exponentially. Thus, at the location $x = 6{\cdot}1$ m, $y = 0$, where the initial reference waves are measured, the waves can be considered close to Stokes waves.

3.2. *Skew waves*

Figure 3(*a*) shows a photographic image of four skew wave patterns that propagate to the right side of the x-axis. Figure 3(*b*) is an annotated line drawing corresponding to figure 3(*a*). The area with lighter tone has waves of lower wave heights than the area with darker tone. Figure 4 shows a clearer view of three-dimensional waveforms of the skew wave groups from the vantage point of the tower at location A (figure 1). The waves between two lighter tone areas (i.e. lower wave height) will be called a skew wave pattern, and each pattern propagates at an angle Ψ with respect to the direction (x-axis) of the initial Stokes wavetrain. The separation distances between two light-tone bands along the x- and y-axes will be called respectively the normal and the crestwise wavelengths of the skew wave patterns λ_{xs} and λ_{ys} (figure 2).

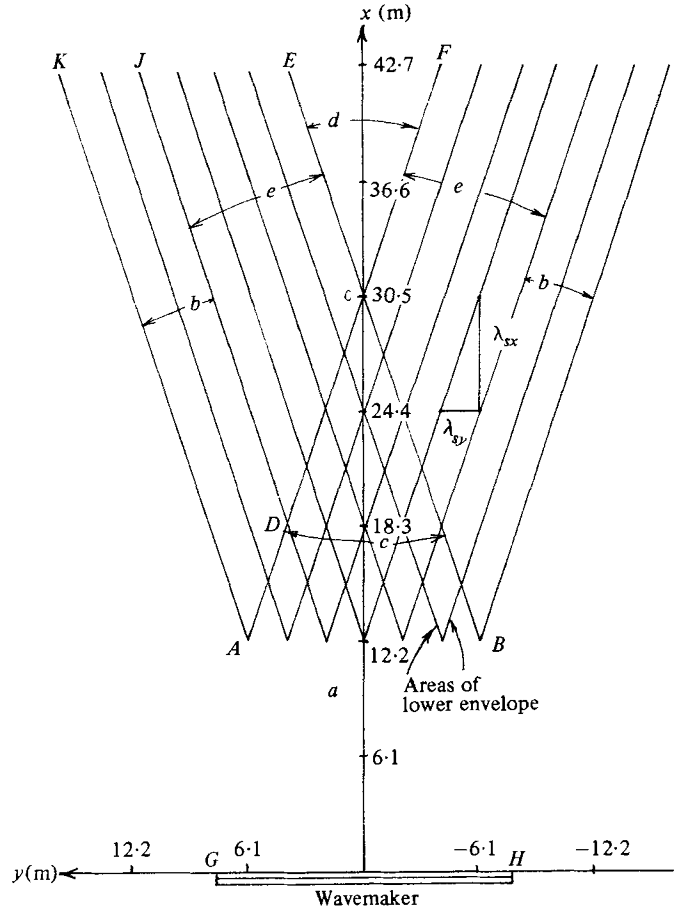

FIGURE 2. A sketch of the overall three-dimensional wave patterns observed in the experiments. *a*, Stokes waves (*ABHG*); *b*, skew wave patterns (*ADJK*); *c*, interactions of skew wave patterns (*ABC*); *d*, Benjamin–Feir modulations of Stokes waves (*ECF*); *e*, Benjamin–Feir modulations of skew waves (*JDCE*).

The travelling velocity of the skew wave pattern normal to the Ψ-direction will be called the pattern velocity C_{ps} of the skew wave pattern. The crestwise wavelength and the propagation angle of the skew wave pattern can be most easily measured from the photographs, utilizing the known co-ordinates of the markers. As an example, in figure 3 (*b*) a light-tone area is seen to extend from point A ($x = 18{\cdot}3$ m, $y = 0$) to point B ($x = 36{\cdot}5$ m, $y = 6{\cdot}1$ m); thus the propagation angle is estimated to be

$$\Psi \simeq \arctan\frac{BC}{AC} = \arctan\frac{20}{120-60} = 18{\cdot}4^\circ,$$

where point C is at $x = 36{\cdot}6$ m, $y = 0$. Next, for estimating λ_{ys} we see that the distance from point D ($x = 24{\cdot}4$ m, $y = 6{\cdot}1$ m) to point E ($x = 24{\cdot}4$ m, $y = 0$) is about $2{\cdot}7\lambda_{ys}$. A more accurate measurement of the crestwise wavelength and the group velocity of the skew wave groups are obtained from the *in situ* surface-displacement measurement by an array of wave-height gauges. Figure 5 (*a*) shows a set of temporal records of surface displacements measured by six wave-height gauges located at $x = 30{\cdot}5$ m,

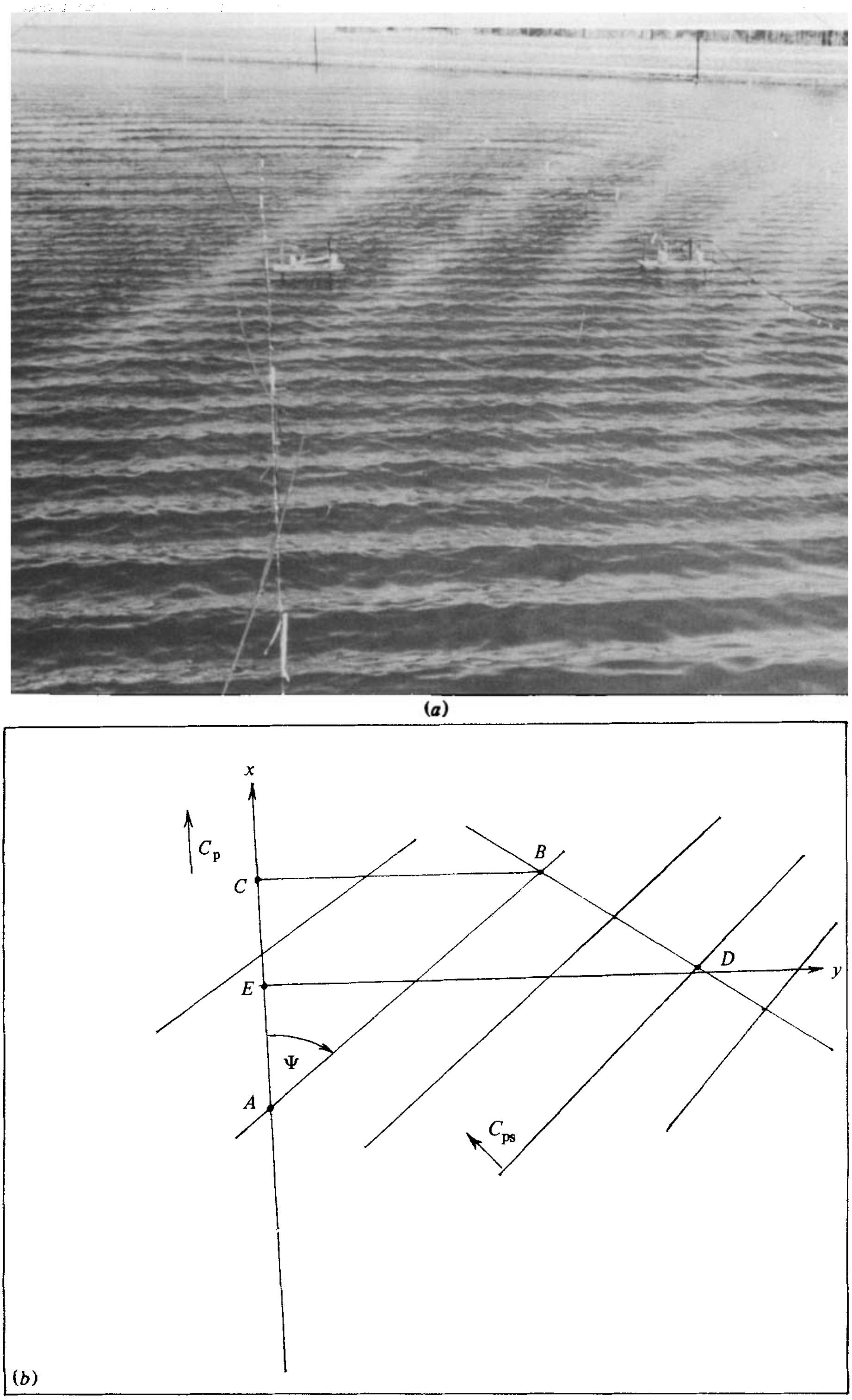

FIGURE 3. (*a*) Image of skew wave patterns with $a_0k_0 = 0{\cdot}17$, $f_0 = 1{\cdot}25$ Hz, $\lambda_0 = 1{\cdot}03$ m. (*b*) Annotation of (*a*) for determining the propagating direction and λ_{sx} and λ_{sy}.

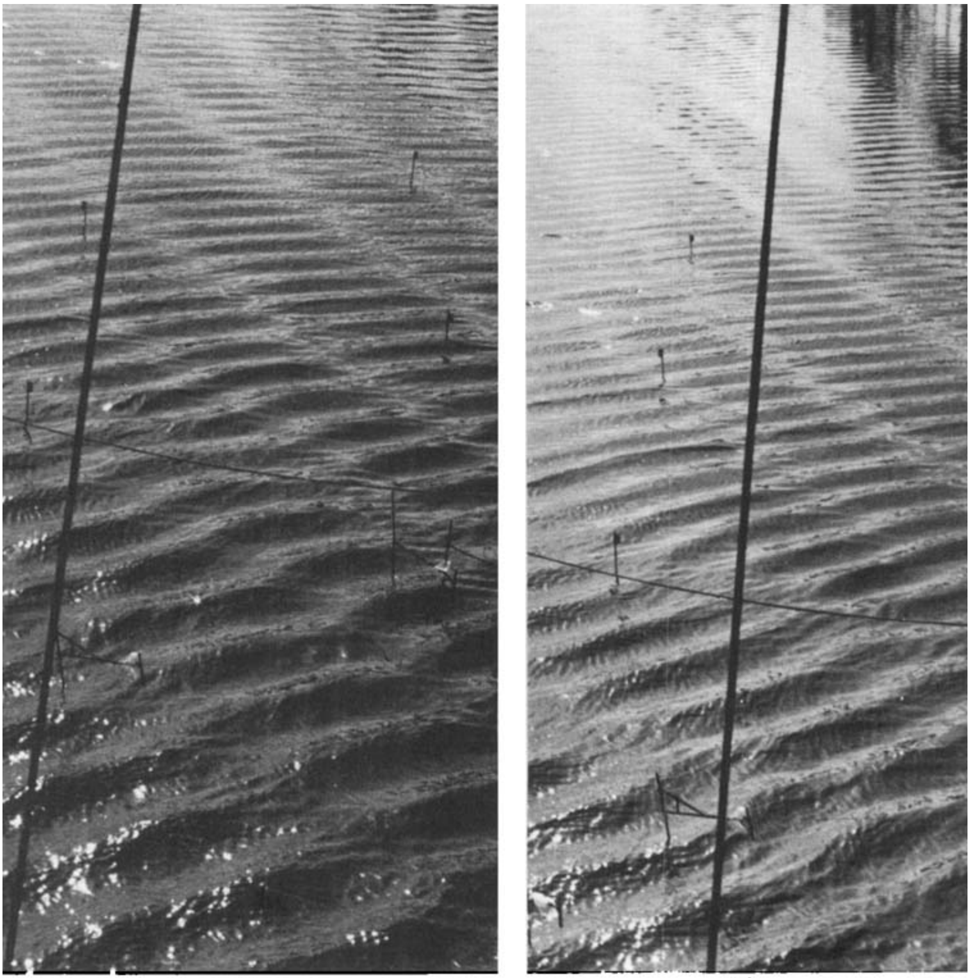

FIGURE 4. Close-up images of skew wave patterns for $a_0k_0 = 0{\cdot}17$.

and $y_i = i\Delta y + 6{\cdot}7$ m ($i = 1, 2, \ldots, 6, \Delta y = 0{\cdot}61$ m). The time interval Δt_{12} between times t_1 and t_2 is the average time for a skew wave group traversing a fixed-location wave gauge. The time interval Δt_{13} between times t_1 and t_3 indicates the time required for the skew wave group to travel a distance of $y = 3{\cdot}05$ m between the first and sixth-wave height gauges in the direction of the y-axis. Thus the corresponding crestwise wavelength and the pattern velocity (normal to the Ψ-direction) are given by

$$\lambda_{ys} = \Delta t_{12}\frac{\Delta y}{\Delta t_{13}} = \frac{\Delta t_{12}}{\Delta t_{13}}\Delta y,$$

$$C_{ps} = \frac{\Delta y}{\Delta t_{13}}\operatorname{cosec}\Psi.$$

For this particular example in figure 5(a), we have

$$\lambda_{ys} = 2{\cdot}84 \text{ m} = 2{\cdot}8\lambda_0,$$

$$C_{ps} = 0{\cdot}035 \text{ m/s} = 0{\cdot}0245C_0.$$

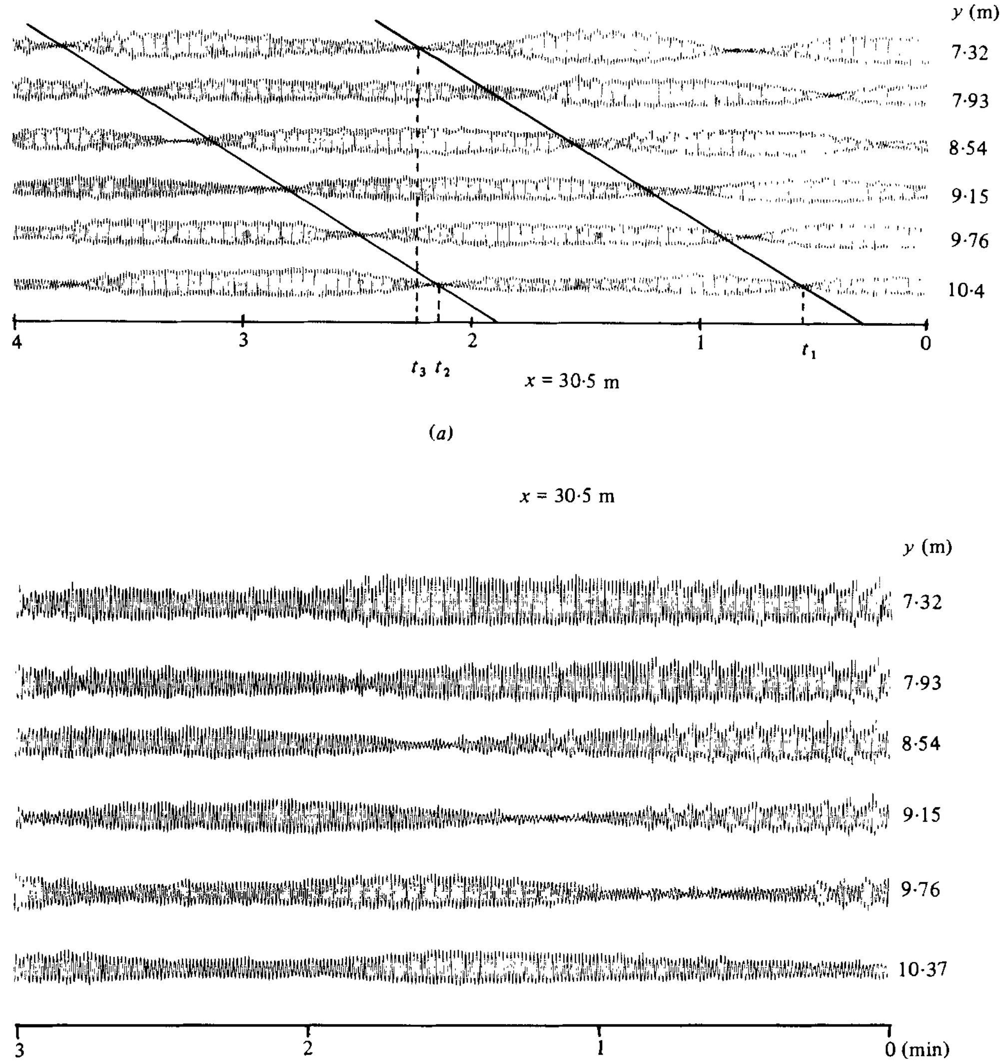

FIGURE 5. (*a*) Six time records of wave profiles measured simultaneously at $x = 30{\cdot}5$ m and (1) $y = 7{\cdot}32$ m, (2) $7{\cdot}93$ m, (3) $8{\cdot}54$ m, (4) $9{\cdot}15$ m, (5) $9{\cdot}76$ m, (6) $10{\cdot}4$ m, showing the 'pure' skew wave pattern. (*b*) Same as (*a*) except that $x = 42{\cdot}7$ m.

Figure 5(*b*) shows a different set of temporal records of surface displacements, which exhibits a slower C_{ps} than that in figure 5(*a*). From the experimental measurements for the initial wave steepness $0{\cdot}16 \lesssim a_0 k_0 \lesssim 0{\cdot}18$, it is found that

$$15^\circ < \Psi < 20^\circ,$$
$$2{\cdot}5\lambda_0 < \lambda_{ys} < 3{\cdot}5\lambda_0,$$
$$\tfrac{1}{35}C_0 < C_{\mathrm{ps}} < \tfrac{1}{65}C_0.$$

Hence the propagation angle Ψ of the skew wave group varies only slightly, with a mean $\Psi = 18{\cdot}5^\circ$, while the crestwise wavelength has a relatively larger variation. The pattern velocity of the skew wave patterns is seen to be about one-fiftieth of the phase velocity of the initial Stokes waves. Thus the skew wave patterns appear almost stationary to an observer standing on the wavemaker.

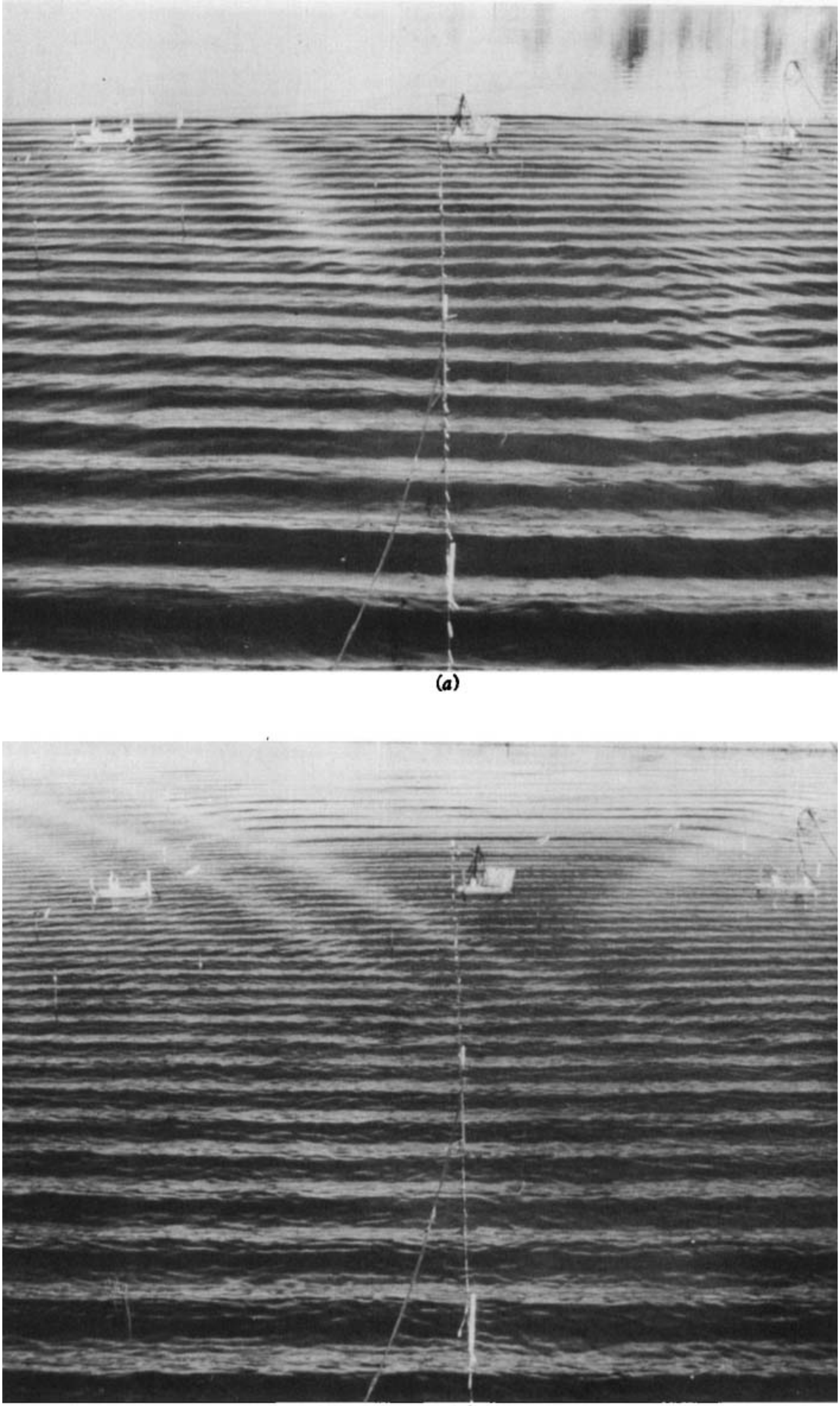

(a)

(b)

FIGURE 6. For caption see facing page.

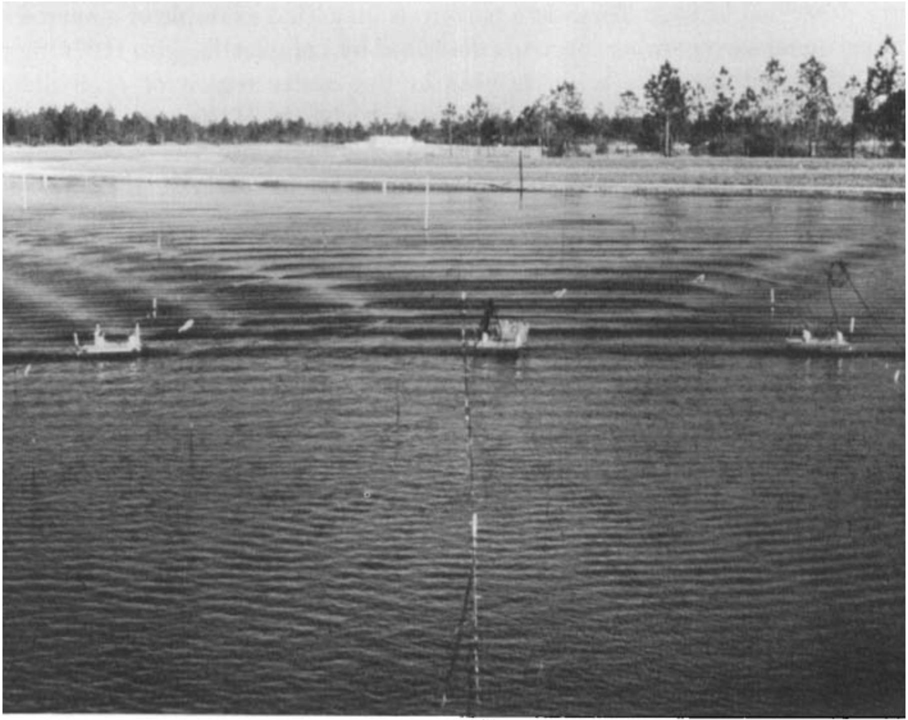

(c)

FIGURE 6. Three stages of evolution of skew wave patterns for $a_0k_0 = 0{\cdot}17$. (*a*) Beginning of the wavetrain. (*b*) Full development of the skew wave patterns. (*c*) Termination of the wavetrain.

Figures 6(*a–c*) show the wave patterns at three consecutive stages of the same wavetrain that produces the skew wave patterns. In all these stages, the leading wavefronts have not reached the side walls of the wide basin. In the first stage (figure 6*a*), when the leading wavefront reached $x = 36{\cdot}6$ m, the skew wave patterns have started to appear. In the second stage (figure 6*b*), when the leading wavefront reached $x = 61$ m, several skew wave patterns are clearly established. In the last stage (figure 6*c*), when the wavetrain was terminated by stopping the wavemaker, the skew wave patterns are seen to extend clearly all the way to the trailing end of the wavetrain (around $x = 30{\cdot}5$ m).

Finally, the envelope $R(t)$ of the wave profiles such as those shown in figure 5(*a*) can be used to estimate the y-direction variation of the wave height over a single skew wave pattern $H(y)$ by applying an appropriate factor:

$$H(y-y_0) = R[C_{\text{ps}}(t-t_0)\sin\Psi].$$

3.3. *Interactions of skew wave patterns*

Referring to figures 2 and 7(*a*, *b*), in the converging cone-shaped area defined by the triangle *ABC* in figure 2, we can see a checkerboard pattern that results from interactions between two sets of the skew wave patterns which propagate in the different directions ($\pm\Psi$). The normal and crestwise dimensions of each diamond-shaped wave pattern are equal to the corresponding dimensions for the 'pure' skew wave patterns described in § 3.2. This wave pattern is an actual example of a narrow-band two-dimensional wavenumber spectrum described by Longuet-Higgins (1976, figure 1). We also observed that the wave heights in the centre region of each diamond-shaped wave pattern are higher than both the wave height of the initial Stokes waves and the '*pure*' skew wave patterns in § 3.2. Furthermore, two sets of the skew wave patterns emerging after the mutual interactions seem to retain their pattern shape without obvious destructive interference. These features may imply that the skew wave pattern, although propagating obliquely from the original Stokes-wave direction, behaves as a pattern of normal Stokes waves. These waves are seen to be stable to finite-amplitude superharmonic disturbances.

3.4. *Benjamin–Feir modulations of Stokes waves*

Referring to figures 2 and 6(*b*) in the diverging core-shape (*ECF* in figure 2) centred on the x-axis, and $y \gtrsim 36{\cdot}6$ m ($35\lambda_0$), we can see predominantly two-dimensional wave-envelope modulations in the direction of the original Stokes waves. These modulations are caused by the two-dimensional side-band instabilities (Benjamin & Feir 1967; Longuet-Higgins 1978). The corresponding group velocity $(C_g)_{\mathrm{BF}}$ of the modulations is roughly one-half of the phase speed, C_0. The corresponding modulational period T_{BF} and the modulational wavelength λ_{BF}, for $a_0 k_0 = 0{\cdot}17$, are $T_{\mathrm{BF}} \simeq 6T_0$ and $\lambda_{\mathrm{BF}} \simeq 3\lambda_0$.

Figure 8 shows two typical time series of wave profiles measured at $x = 42{\cdot}7$ m ($42\lambda_0$) and $x = 54{\cdot}9$ m ($54\lambda_0$), $y = 0$. The envelope modulations of every 5 to 6 wave periods clearly show up in the first time series, as expected, while more irregular modulations are shown in the second time series. The latter phenomenon is related to a significantly different long-time behaviour of the side-band instabilities, which effectively shift the peak frequency of the spectrum of the original unstable wave-train to a lower frequency (Su 1981).

3.5. *Benjamin–Feir modulations of skew waves*

Referring to figures 2 and 6(*b*, *c*), in the region overlapped by the pure skew waves and the Benjamin–Feir modulations of Stokes waves, we can see a series of compact three-dimensional wave groups which are results of interactions between the above two characteristically different waveforms. These compact wave groups assume shapes of a skewed diamond. The normal wavelength is the same as for the Benjamin–Feir modulation of Stokes waves, while the crestwise wavelength is the same as for the 'pure' skew wave patterns. The gross appearance of the envelope of the compact wave group seems to indicate that the different characteristics of the skew waves and Benjamin–Feir modulations are not affected by their spatial co-existence. Figure 9 shows a set of six time series of wave profiles measured within the mixed regime. Two types of envelope modulations can be seen clearly; one with a period about $6T_0$, and the other with a period about $150T_0$. The shorter-period modulations with a marked symmetry are caused by Benjamin–Feir instabilities, while the longer modulations are due to the much slower movement of the skew wave pattern (see § 3.2).

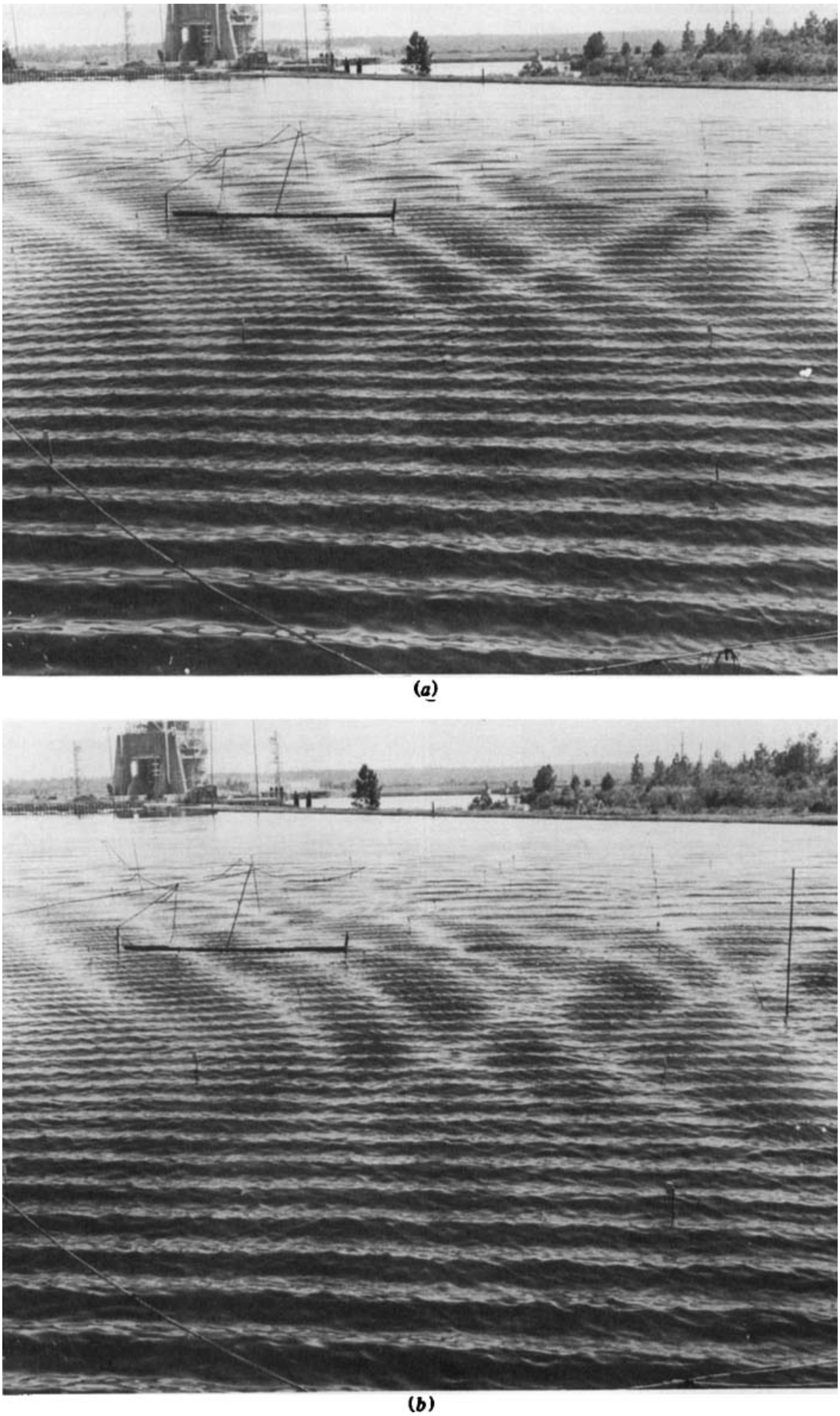

FIGURE 7. Two photographic images of interactions of skew wave patterns propagating from different directions $\Psi = \pm 18°$.

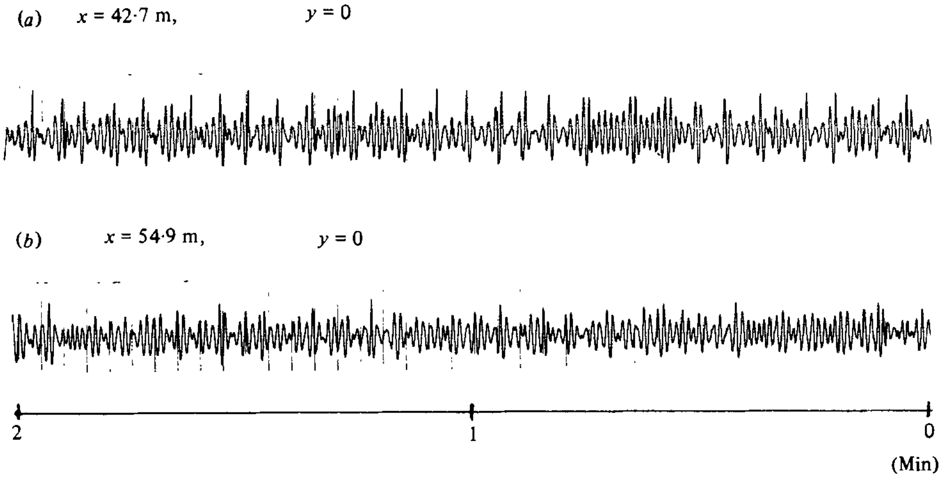

FIGURE 8. Two time records of wave profiles for $a_0 k_0 = 0{\cdot}17$ at (a) $x = 42{\cdot}7$ m, $y = 0$, and (b) $x = 54{\cdot}9$ m, $y = 0$, showing the modulational envelope due to Benjamin–Feir instability.

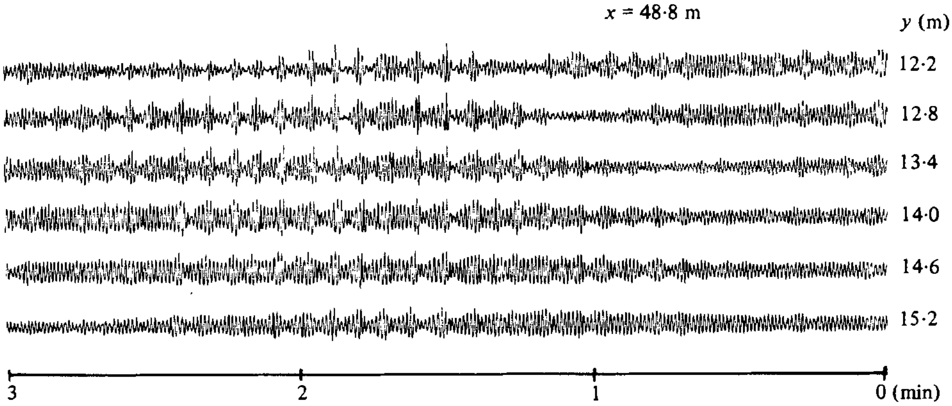

FIGURE 9. Six time records of wave profiles for $a_0 k_0 = 0{\cdot}17$ at $x = 48{\cdot}8$ m, and $y = 12{\cdot}2$ m to 15·3 m with 0·61 m separation, showing the interaction of skew waves (longer modulations) and Benjamin–Feir modulation (shorter modulations).

Rather than regarding the phenomenon as the *interaction* of the two types of wave patterns, it may be physically more accurate to state that the skew waves, just like the regular Stokes waves, are unstable to the subharmonic side-band instability. Furthermore, with the initial wave steepness near $a_0 k_0 = 0{\cdot}17$, the growth rates for the side-band instability and the bifurcation of the Stokes waves to the skew waves are about the same. We note that the skew waves are observed clearly in our experiment only in a fairly narrow range of steepness, i.e. $0{\cdot}16 \gtrsim a_0 k_0 \lesssim 0{\cdot}18$, and that the predominantly two-dimensional envelope modulations of Benjamin–Feir instability show rather uniformly over a wider range of steepness, i.e. $0{\cdot}1 < a_0 k_0 < 0{\cdot}25$ (Longuet-Higgins 1978; McLean *et al.* 1980; Su 1981). These observations would imply that the bifurcation rate for the skew waves would be much lower than the growth rate of the Benjamin–Feir instability for $a_0 k_0 < 0{\cdot}16$ and $a_0 k_0 > 0{\cdot}18$. Finally, we note another difference between the skew waves and the side-band modulation; the former, developed from the bifurcation, remains fairly steady in form over $100\,T_0$, while the latter is

FIGURE 10. Three-dimensional symmetric waves of L_2 configuration observed in the wide wave basin; $f_0 = 1{\cdot}2$ Hz, $a_0k_0 = 0{\cdot}33$.

intrinsically transient, and transforms to a wavetrain with lower carrier frequency over about $50T_0$.

4. Structures of symmetric wave patterns

4.1. *Configurations of wave patterns*

For clarity of the description of observations which follow, we define the characteristic scales of the wave field. The wavetrain is initially composed of waves with length λ_0, amplitude a_0, wavenumber $k_0 = 2\pi/\lambda_0$ and frequency f_0. The three-dimensional symmetric waves have crestwise wavelength λ_{BC} and their subharmonic periodicity is $L_m = m\lambda_0$ ($m = 2, 3, 4, \ldots$). The initial wave steepness is a_0k_0.

Figure 10 shows a typical example of crescent-shaped symmetric waves in the wide basin ($1 \times 100 \times 340$ m) for the conditions $f_0 = 1{\cdot}2$ Hz, $a_0k_0 = 0{\cdot}33$, $\lambda_0 = 1{\cdot}08$ m and $\lambda_{\mathrm{BC}} = 0{\cdot}915$ m. Figures 11 and 12 represent typical symmetric waves with the same initial parameters as shown in figure 10, but are observed in a tow tank ($3{\cdot}66 \times 3{\cdot}66 \times 137$ m).

In all of our measurements only three distinct spatial configurations of symmetric waves occur. The first and most frequent configuration is denoted as $L_2 = 2\lambda_0$, and is sketched in figure 12. Figure 12(*a*) represents the top view of wave crests. The example given in figure 10 belongs to this category. Note that the crests are shifted by one-half of the width of the crescents ($\frac{1}{2}\lambda_{\mathrm{BC}}$) on successive rows. I and II in figure 12(*b*) are typical profiles observed at $y = 0$ and $y = \frac{1}{4}\lambda_{\mathrm{BC}}$, i.e. at crescent centre and quarter-width respectively. The corresponding maxima (crests) and minima (troughs)

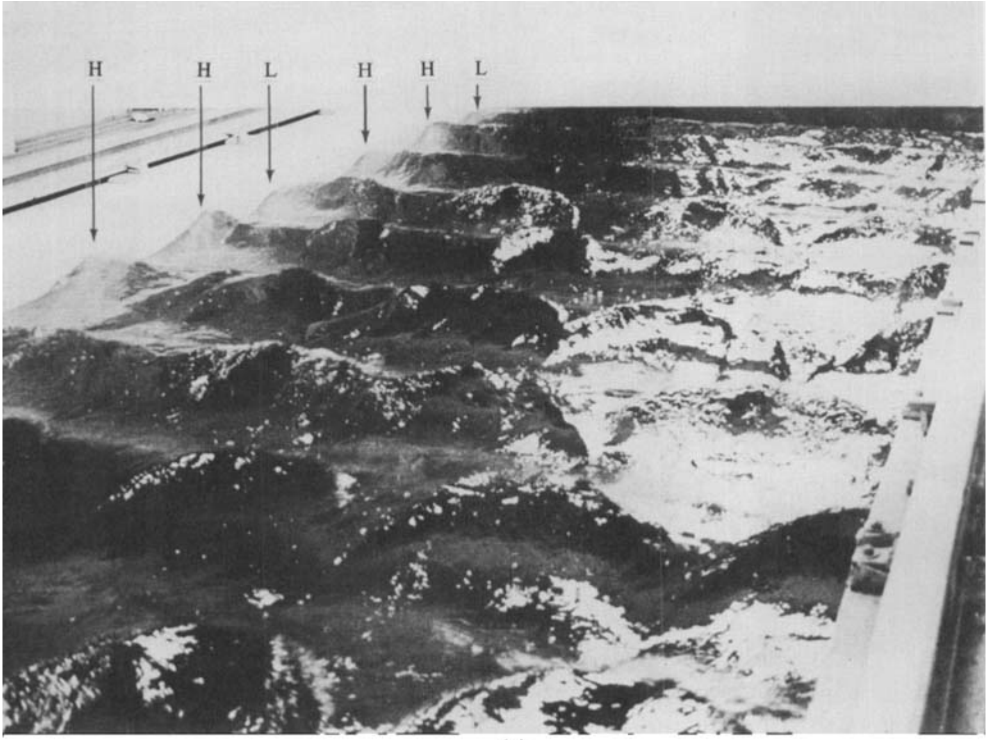

(a)

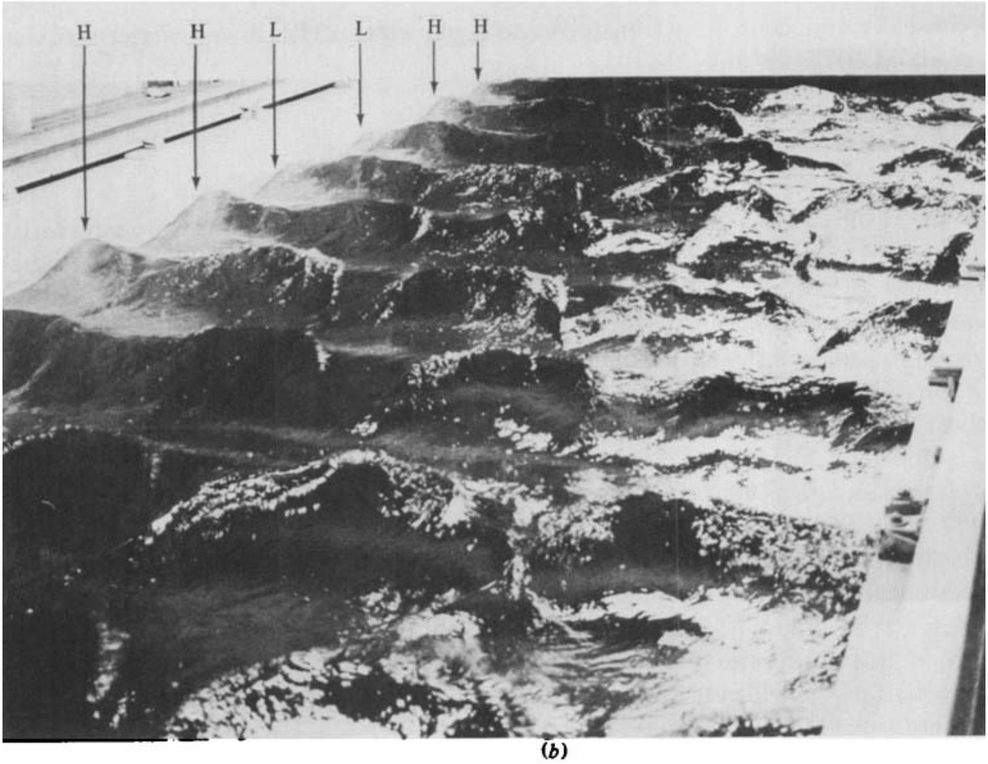

(b)

FIGURE 11. Two examples of three-dimensional symmetric waves of L_3 and L_4 configurations observed in the tow tank: $f_0 = 1{\cdot}2$ Hz and $a_0k_0 = 0{\cdot}33$. The letters H and L are used to point out the high and low crests, respectively.

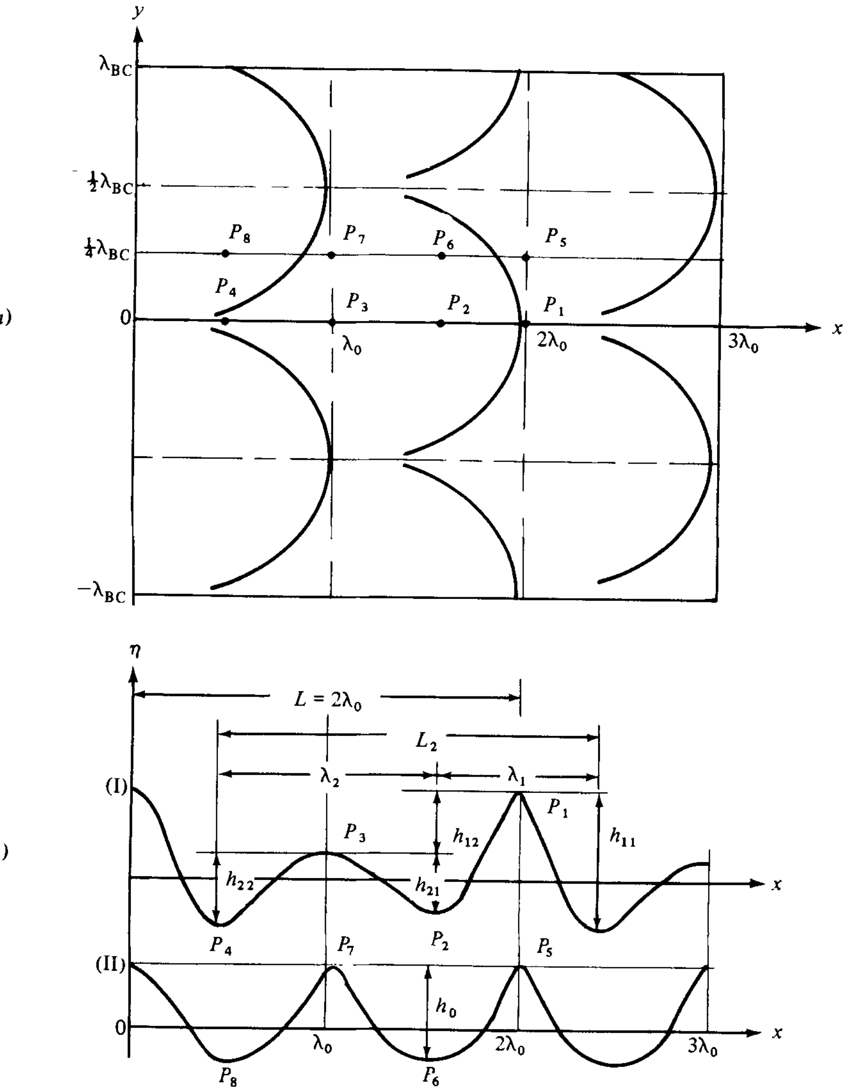

FIGURE 12. Definition sketch of L_2 configuration of symmetric waves. (a) Top view of wave crests. (b) Wave profiles along $y = 0$ (I) and along $y = \frac{1}{4}\lambda_{BC}$ (II).

occur at P_i ($i = 1, 2, \ldots, 8$). The trough at P_4 is deeper than the trough at P_2. The wave profile II in figure 12 exhibits less distortion than the profile I, and is similar to the form measured close to the wavemaker. A set of records obtained from 13 gauges at intervals of 4 cm ($\simeq \frac{1}{24}\lambda_{BC}$) over the range $y = 0$ to $y = \frac{1}{2}\lambda_{BC}$ is presented in figure 13. Wave profiles (a) and (m) in figure 13 correspond to the sketch profile I in figure 12(b) and the wave profile (g) in figure 13 corresponds to II.

The second configuration of the symmetric waves characterized by the subharmonic scale $L_3 = 3\lambda_0$ is sketched in figure 14. Figure 14(a) is the top view of the crests. The corresponding typical profiles for $y = 0$ and $y = \frac{1}{2}\lambda_{BC}$ are represented respectively by I and II in figure 14(b). Note that every third row of symmetric waves has a $\frac{1}{2}\lambda_{BC}$ crestwise shift with respect to the other two rows. These sketches

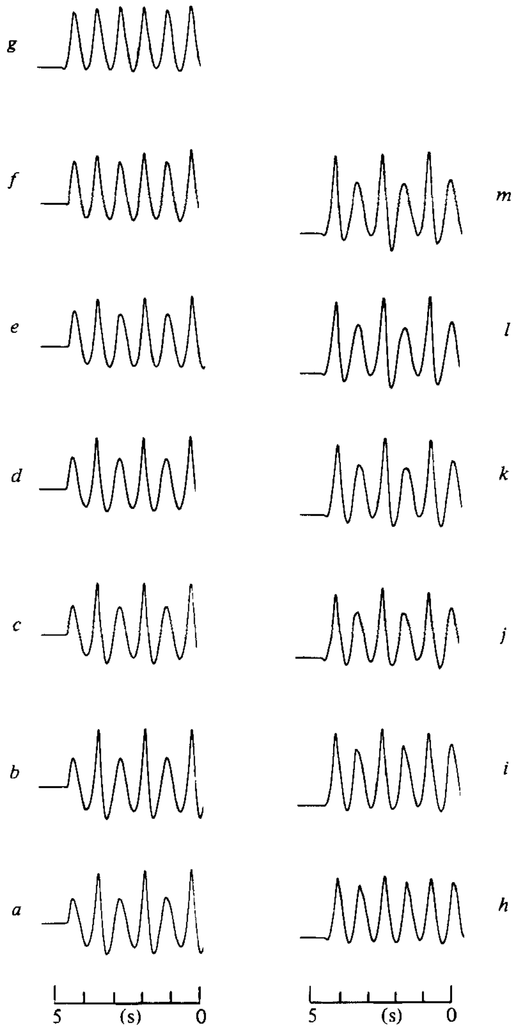

FIGURE 13. Measurement of wave profiles for L_2 configuration at points, a ($y = 0$) to m ($y = \lambda_B$) with an equal increment $\Delta y = 4$ cm $= \frac{1}{24}\lambda_{BC}$.

represent wave patterns which are noted by arrows in figure 11. Records of wave profiles for this configuration are presented in figure 15. The distribution of sensors is identical with that used to obtain the results in figure 13.

The third configuration characterized by $L_4 = 4\lambda_0$ is sketched in figure 16. The wave fields as seen from above are shown in figure 6(a), and the corresponding wave cross-sections at $y = 0$ and $y = \frac{1}{2}\lambda_{BC}$ are represented by I and II in figure 16(b). In this case, two rows of symmetric waves with the same crestwise relationship are followed by two other rows of the same kind, but with a $\frac{1}{2}\lambda_{BC}$ crestwise shifting between these two pairs. The L_4 configuration is geometrically equivalent to the L_2 configuration, with doubling each row of symmetric waves of the latter. Measurements of wave profiles for this case are given for the second to the fifth waves in figure 17. The distribution of sensors is the same as that used in figure 13.

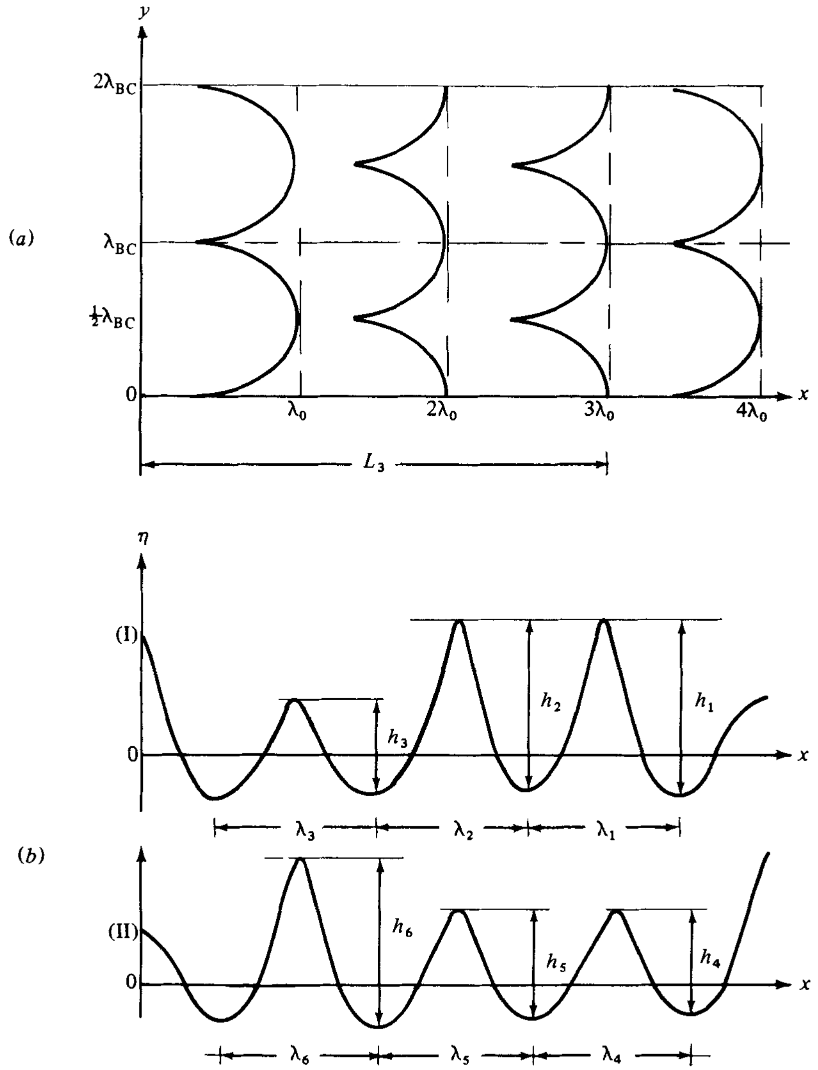

FIGURE 14. Definition sketch of L_3 configuration of symmetric waves; (*a*) Top view of wave crests. (*b*) Wave profiles along $y = 0$ (I) and along $y = \frac{1}{2}\lambda_{BC}$ (II).

The records in figure 17 include all three types of symmetric wave configurations described thus far. A rough estimate based on experimental measurements indicates that the L_2 configuration occurs more than 90 % of the time, and that the L_3 and L_4 configurations have less than 10 % and 1 % incidence of occurrences respectively. In view of the very low probability of occurrence for the L_4, we shall discuss only the conditions under which L_2 and L_3 are present.

4.2. *Height and slope structures*

Since all the symmetric waves observed in the experiments for the range of initial steepness ($0{\cdot}25 < ak < 0{\cdot}34$) of steep deep-water gravity wavetrains have similar profiles, we shall use some typical examples to represent their structures. The surface

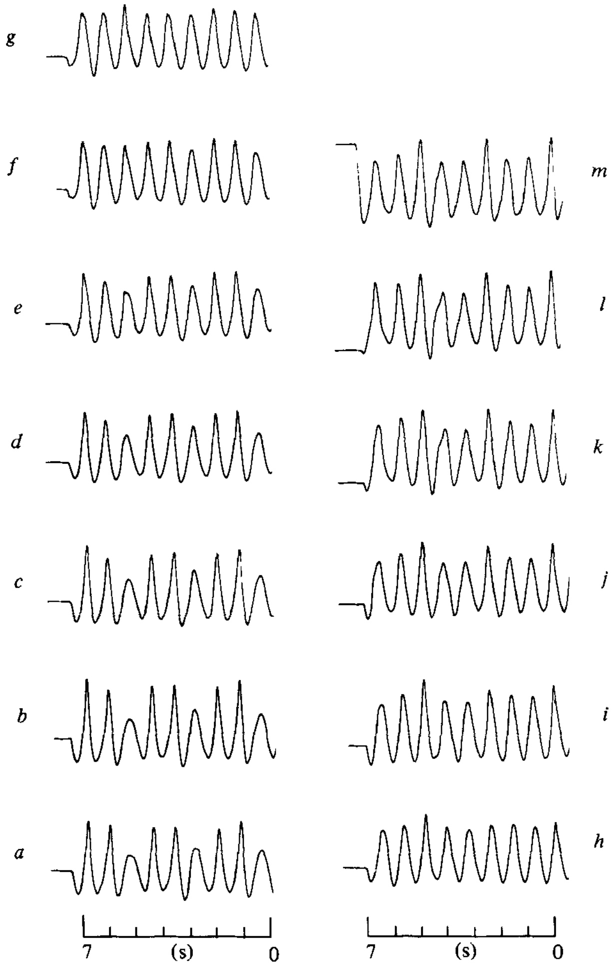

FIGURE 15. Measurement of wave profiles for L_3 configuration at *a* ($y = 0$) to *m* ($y = \frac{1}{2}\lambda_{BC}$) with an equal increment $\Delta y = 4$ cm $= \frac{1}{24}\lambda_{BC}$ for the interim profiles *b* to *l* respectively.

slope S_x in the direction of wave propagation is computed from the digital wave-height records:

$$S_x = \left.\frac{\partial \eta}{\partial x}\right|_y \simeq \frac{\eta(t+\Delta t)-\eta(t)}{c\Delta t}, \tag{1}$$

where $\eta = \eta(x, y)$ is the water-surface elevation at location (x, y), c is the phase speed of the waves and Δt is the time interval between two digital samples, which is $\frac{1}{40}$ s in our measurements. Since the time scale of appearance of the three-dimensional symmetric waves is about ten wave periods, which are equal to 0·83 s, the surface slope, as computed by the above approximation, would be subject to less than 1 % error due to the assumption of frozen pattern. The presence of small capillary waves and a meniscus around the wave-height sensor element would limit any higher accuracy in computing surface slopes.

We must now explain why we used the phase speed c, rather than the group speed in (1) for estimating the surface slope of the symmetric waves. This was based on both the experimental observation that the three-dimensional symmetric waves move at the same speed of the underlying two-dimensional fundamental waves, and on the

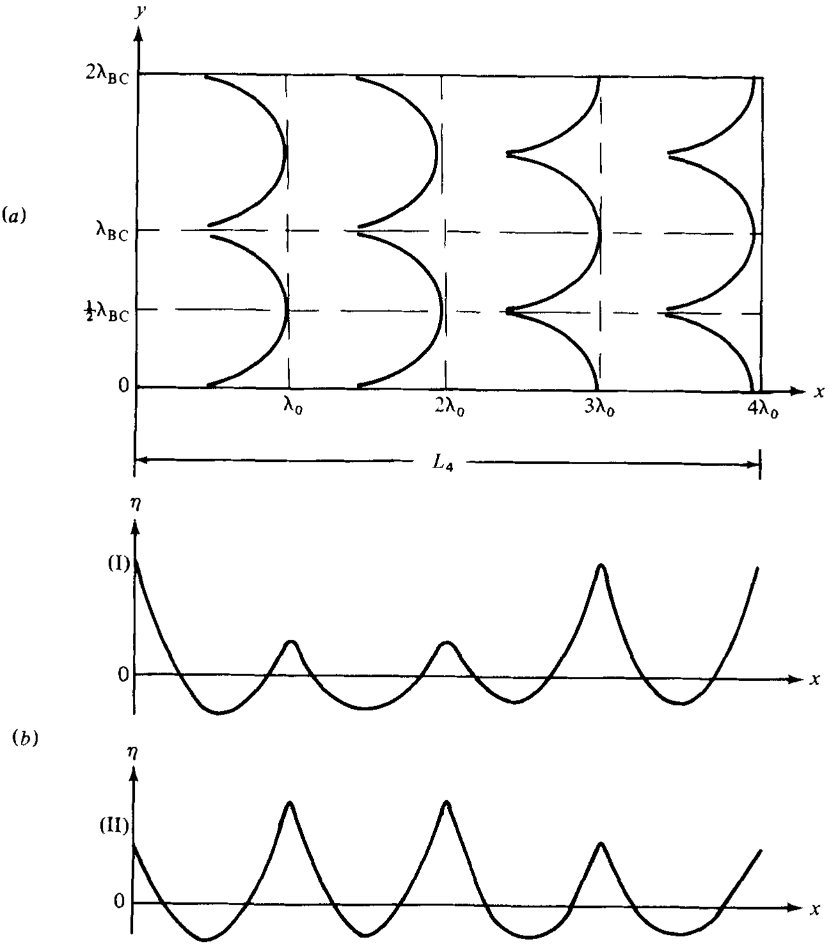

FIGURE 16. Definition sketch of L_4 configuration of symmetric waves. (a) Top view of wave crests. (b) Wave profiles along $y = 0$ (I) and along $y = \frac{1}{2}\lambda_{\mathrm{BC}}$ (II).

theoretical characteristics of the three-dimensional instabilities (see § 5 for more discussions).

As a reference, we first give an example of the waveforms at $x = 6{\cdot}1$ m ($\simeq 5{\cdot}6\lambda_0$ from the wavemaker). The pertinent parameters are $f_0 = 1{\cdot}2$ Hz, wavelength $\lambda_0 = 1{\cdot}08$ m and wave height $H_0 = 2a_0 = 11{\cdot}5$ cm, with wave steepness $a_0k_0 = 0{\cdot}33$. The crest-wise wavelength of the symmetric waves, which is most distinct at $x = 27{\cdot}5$ m ($\simeq 25{\cdot}5\lambda_0$), is $\lambda_{\mathrm{BC}} = 0{\cdot}915$ m. Figures 18 (a, b) show the temporal record of surface displacement and the corresponding local surface slope in the direction of wave propagation at $y = 0$ to $y = \frac{1}{2}\lambda_{\mathrm{BC}}$, with an equal increment of $\Delta y = 4$ cm (see figure 12 for definition of the co-ordinate system). Close similarity among the 13 curves in figures 18 (a, b) demonstrates not only the two-dimensionality of the initial waveform, but also the consistency among the 13 wave-height sensors used in the experiments. For clarity, we have replotted the surface displacement and its corresponding surface slope in figure 18 (c) for one particular sensor at $y = \frac{1}{2}\lambda_{\mathrm{BC}}$. Note that the maximum S_x is about 0·45, which is about 20 % lower than Stokes limiting slope at the cusp of the crest $(S_x)_{\mathrm{m}} = \cos 30° = 0{\cdot}577$.

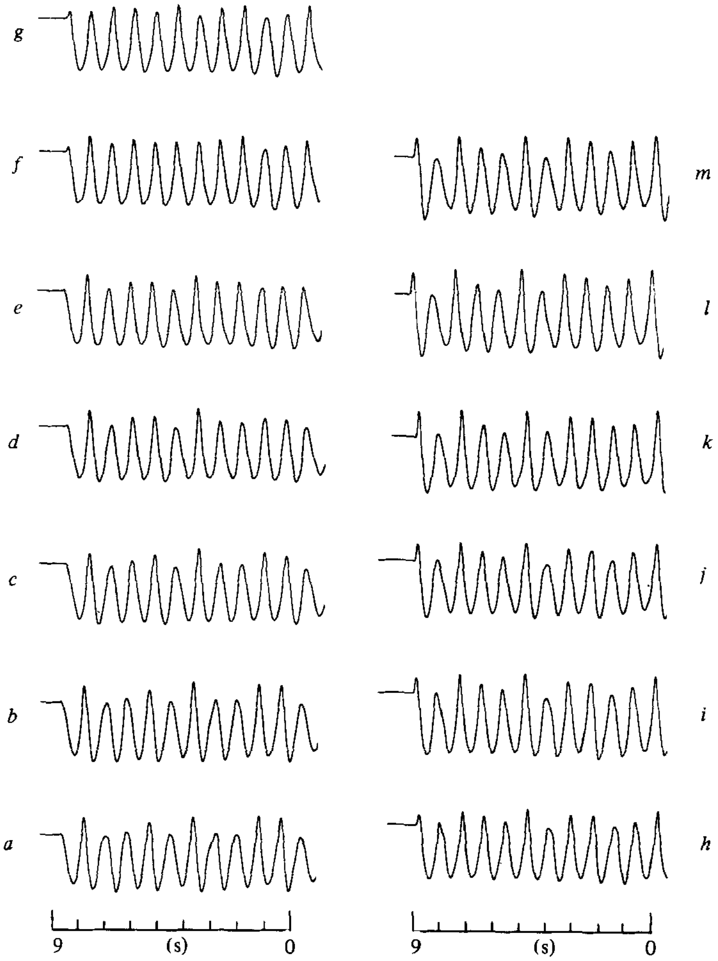

FIGURE 17. Measurement of wave profiles for mixed L_4, L_2 and L_3 configurations with other labels same as in figure 00.

Figures 19(*a*, *b*) present the surface displacement and local surface slope for the L_2 configuration of symmetric waves. For clarity seven of these series are replotted in figure 20(*a*–*g*). Along the wave profile at $y = 0$ (figure 20*a*), the forward faces of the higher waves are seen to be steeper than the rear face. The maximum S_x on the forward face is 0·65 in figure 20(*a*), and 1·02 in figure 20(*e*); they exceed $(S_x)_{\mathrm{m}}$. It is believed that this is the result of the three-dimensionality of the symmetric waves. The slope of the forward face of the lower wave is about the same as the rear face, and the maximum S_x is about 0·33, which is lower than the maximum slope of the initial waves (0·45). Other parameters defined in figure 12 and some characteristic ratios of interest are (along $y = 0$)

$$\lambda_1 = 94{\cdot}6 \text{ cm}, \quad \lambda_2 = 121{\cdot}4 \text{ cm}, \quad \lambda_2/\lambda_1 = 1{\cdot}28,$$

$$h_{11} = 13{\cdot}3 \text{ cm}, \quad h_{12} = 12{\cdot}1 \text{ cm}, \quad h_{21} = 8{\cdot}0 \text{ cm}, \quad h_{22} = 9{\cdot}1 \text{ cm},$$

$$\frac{h_{11}}{h_{12}} = 1{\cdot}1, \quad \frac{h_{11}}{h_{21}} = 1{\cdot}66, \quad \frac{h_{11}+h_{12}}{h_{21}+h_{22}} = 1{\cdot}49, \quad \frac{h_{21}}{h_{22}} = 0{\cdot}88.$$

Along $y = \frac{1}{4}\lambda_{\mathrm{BC}}$ (figure 20*g*) both the surface displacement and the slope are similar to those at $x = 6{\cdot}1$ m (figure 18*c*).

Figures 21(*a*, *b*) present the plots of surface displacement and local slope, respectively, for the L_3 configuration. For clarity three sets of corresponding surface displacement and slope are given in figure 22(*a*–*c*). Note that the waveform shows two high waves and one low wave along $y = 0$, and one high wave and two low waves along $y = \frac{1}{2}\lambda_{\mathrm{BC}}$. Along $y = 0$, the maximum values of S_x of the forward and rear faces of the first high wave are 0·655 and 0·495 respectively; the corresponding values for the second high wave are 0·55 and 0·47, and those for the lower waves are 0·235 and 0·32. Along $y = \frac{1}{2}\lambda_{\mathrm{BC}}$, the maximum values of S_x of both the forward and rear faces of the first low wave are 0·24 and 0·29 respectively; the corresponding values for the second low wave are 0·25 and 0·31; and those for the higher wave are 1·1 and 0·60. These typical values of local surface slope thus show that the overall maximum local slope occurs on the forward face of the high wave along $\lambda = \frac{1}{2}\lambda_{\mathrm{BC}}$. Other parameters of interest as defined in figure 14 and their ratios are

$$\lambda_1 = 103\ \mathrm{cm}, \quad \lambda_2 = 96{\cdot}6\ \mathrm{cm}, \quad \lambda_3 = 124{\cdot}4\ \mathrm{cm},$$
$$h_1 = 12{\cdot}2\ \mathrm{cm}, \quad h_2 = 10{\cdot}6\ \mathrm{cm}, \quad h_3 = 7{\cdot}2\ \mathrm{cm},$$
$$\frac{h_1}{h_2} = 1{\cdot}7, \quad \frac{h_2}{h_3} = 1{\cdot}47, \quad \frac{\lambda_1}{\lambda_3} = 0{\cdot}83, \quad \frac{\lambda_2}{\lambda_3} = 0{\cdot}78.$$

Comparing the maximum local slopes between the L_2 and L_3 configurations, the highest local slope is found to occur in the latter configuration, and its values exceed the Stokes limiting slope $(S_x)_{\mathrm{m}}$ by more than 70 %. This effect is attributed to the three-dimensional structure of the symmetric waves.

4.3. *Amplitude spectra of symmetric waves*

Next we examine the spatial variations of amplitude spectra computed from time series of surface elevation in the L_2 and L_3 configurations.

Assume that the initial waves near the wavemaker have the basic frequency f_0, and higher harmonics with

$$f_n = nf_0 \quad (n = 1, 2, 3, \ldots).$$

Then the L_2 configuration, which has a periodicity of two wavelengths along $y = 0$, will contain additional frequency components

$$\tilde{f}_m = \tfrac{1}{2}(2m+1)f_0 \quad (m = 0, 1, 2, 3, \ldots).$$

There will be a new subharmonic component $\tilde{f}_0 = \frac{1}{2}f_0$, as well as a series of new superharmonic components $\tilde{f}_m$ $(m = 1, 2, 3)$ distributed about mid-frequency between the original harmonics f_n. Similarly, for the L_3 configuration, which has a periodicity of three wavelengths, additional new components are

$$\tilde{\tilde{f}}_0 = \tfrac{1}{3}f_0, \quad \tilde{\tilde{f}}_m = \tfrac{1}{3}(3m+1)f_0.$$

When a waveform is a mixture of L_2 and L_3 configurations, all of the wave components with $f_n, \tilde{f}_m$ and $\tilde{\tilde{f}}_m$ are found in the computed amplitude spectrum. This heuristic model is consistent with measurements of the amplitude spectra, which are the amplitudes of the Fourier transform of the time series of wave records at seven equally spaced locations from $y = 0$ to $y = \frac{1}{4}\lambda$, with $\Delta y = 4$ cm (figure 23). Note that the wave profile

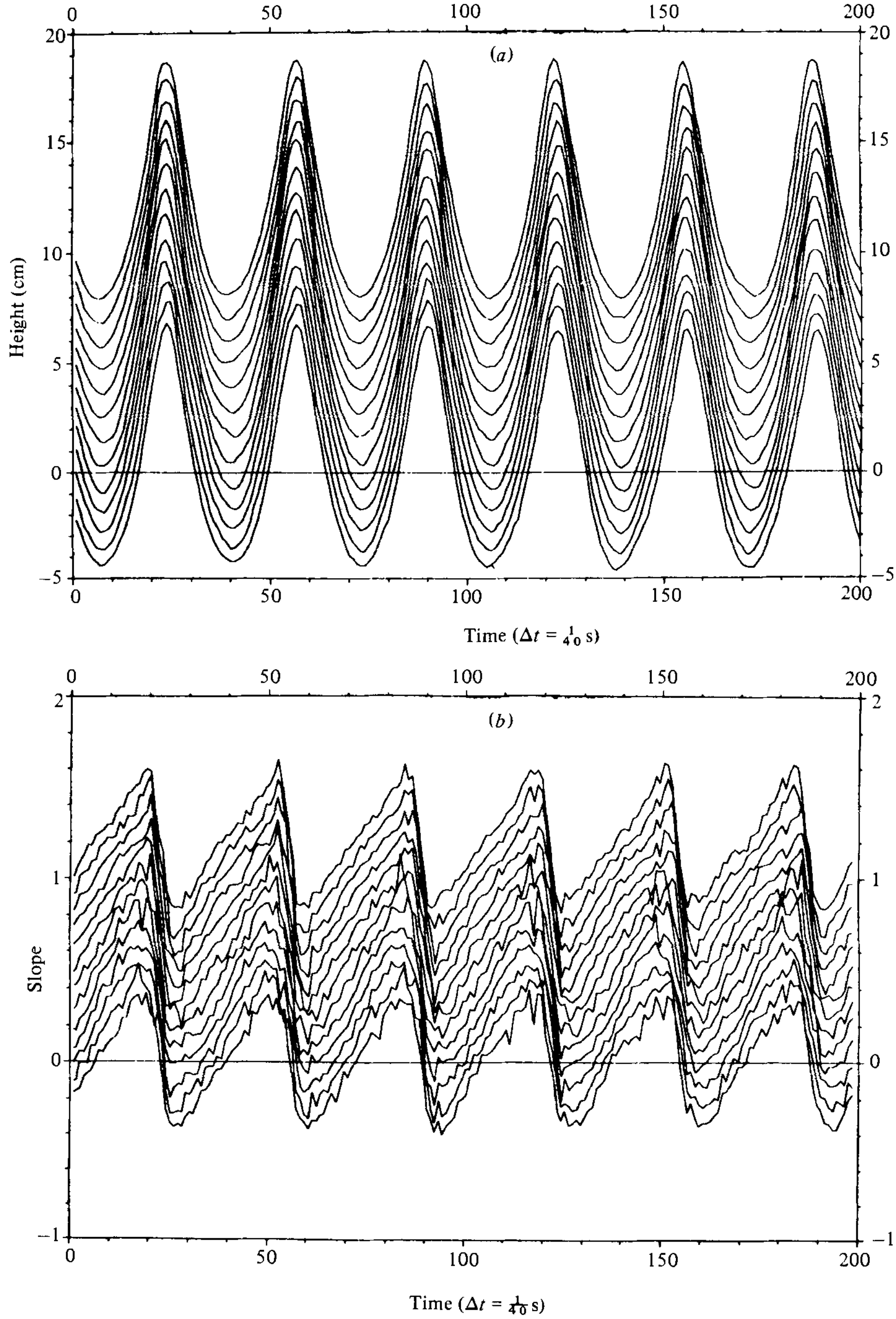

FIGURE 18. For caption see facing page.

at $y = \frac{1}{4}\lambda_{BC}$ is similar to the initial waveform (figure 18*c*); thus the corresponding amplitude spectrum consists of only the basic wave component with $f_0 = 1{\cdot}2$ Hz, plus three harmonics at $f_1 = 2{\cdot}4$ Hz, $f_2 = 3{\cdot}6$ Hz and $f_3 = 4{\cdot}8$ Hz, with the rest being very small. The wave profile along $y = 0$ is a mixture of more than 90 % of the L_2 configurations and less than 10 % of the L_3 configurations; thus the corresponding

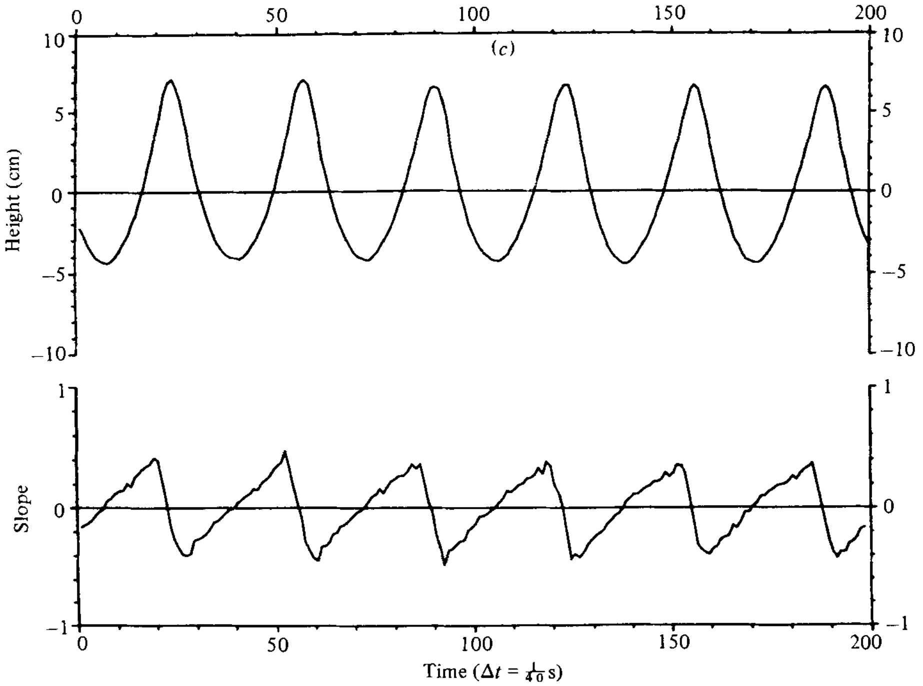

FIGURE 18. (*a*) Plots of wave profiles for $y = 0$ to $y = \frac{1}{2}\lambda_{BC}$ with $y = 4$ cm $\simeq \frac{1}{24}\lambda_{BC}$ for initia waves at $x = 6{\cdot}1$ m; $f_0 = 1{\cdot}2$ Hz, $a_0k_0 = 0{\cdot}33$. The horizontal scale is $\Delta t = \frac{1}{40}$ s. The bottom wave profile is plotted to the vertical ordinate and the others are translated by 1 cm successively. (*b*) Plots of surface slope corresponding to the wave profiles in (*a*). The lowest curve is plotted for values of the true ordinate and the other curves are offset vertically by $0{\cdot}1$ successively. (*c*) Plots of corresponding surface displacement and surface slope for one location of $y = \frac{1}{2}\lambda_{BC}$ of (*a*) and (*b*).

amplitude spectrum shows the wave components at $\tilde{f}_1 = 1{\cdot}8$ Hz, $\tilde{f}_2 = 3{\cdot}0$ Hz, $\tilde{f}_3 = 4{\cdot}2$ Hz and $\tilde{f}_4 = 5{\cdot}4$ Hz, in addition to those at f_0, f_1, f_2, f_3 and f_4.

5. Interpretation and comparison with theory

We shall now give an interpretation of the skew and symmetric waves by comparing our observations with the theoretical computations by Saffman & Yuen (1980) and Meiron *et al.* (1982), who predict the existence of such waves based on the Zakharov equation, which is valid for weakly nonlinear waves (Zakharov 1968), and with the new type of three-dimensional instability discussed by McLean *et al.* (1980) and McLean (1982).

Are the experimentally observed skew waves the same as the theoretical prediction of Saffman, Yuen and Meiron? Before answering this question, we would like to rule out two other more obvious explanations that will be shown to be incompatible with the wave phenomenon under consideration. The first explanation is to regard these skew waves as regular standing wave patterns resulting from superposition of the original Stokes waves and some reflected waves from the side walls of the wide basin. In figure 6 (*c*) the skew waves are seen to extend all the way to the trailing edge of the terminated wavetrain. If reflected waves with a frequency and amplitude comparable

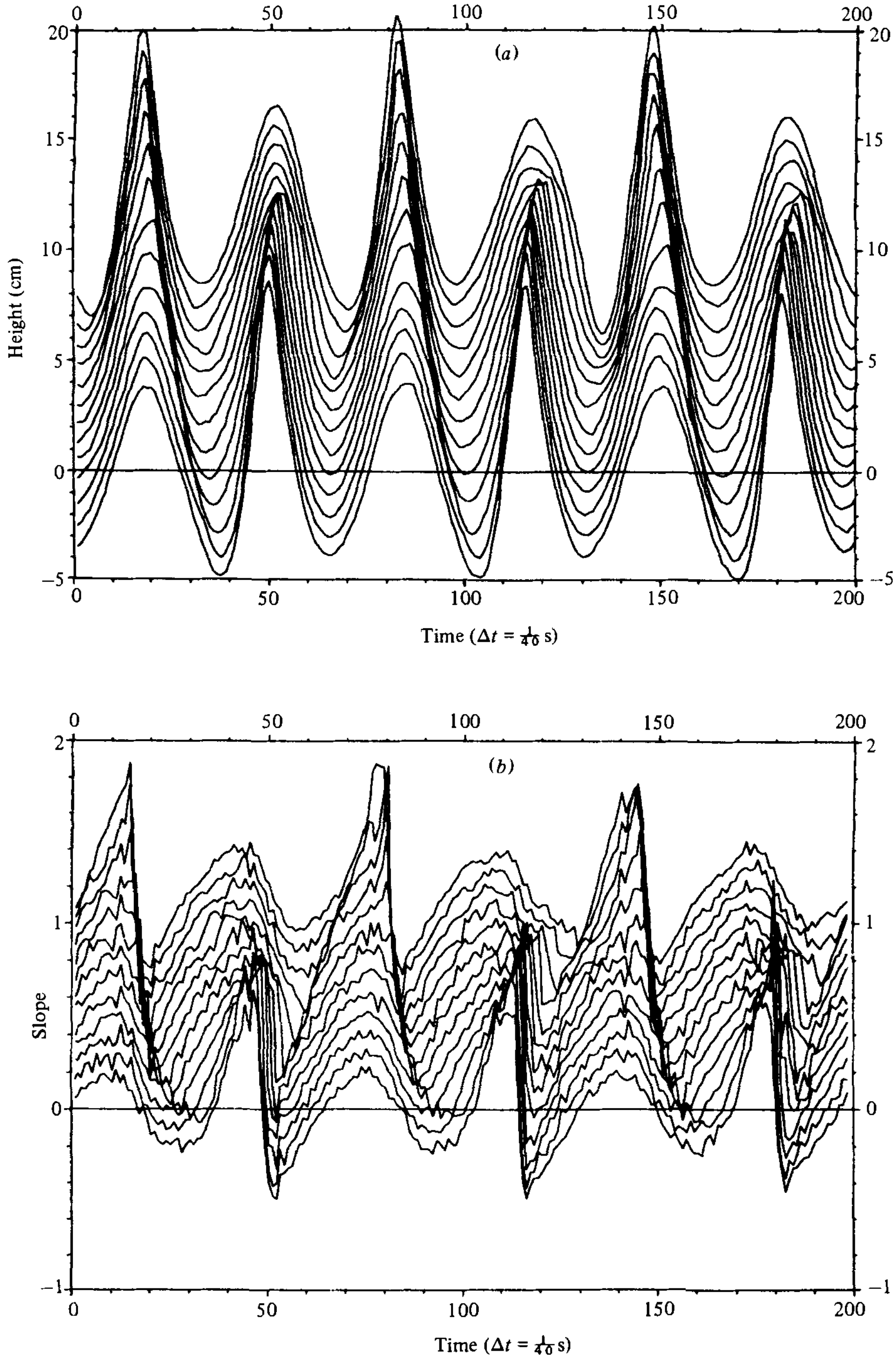

FIGURE 19. (*a*) Plots of wave profiles for L_2 configuration of symmetric waves. The method of presentation is the same as in figure 18(*a*). (*b*) Plots of surface slopes corresponding to (*a*).

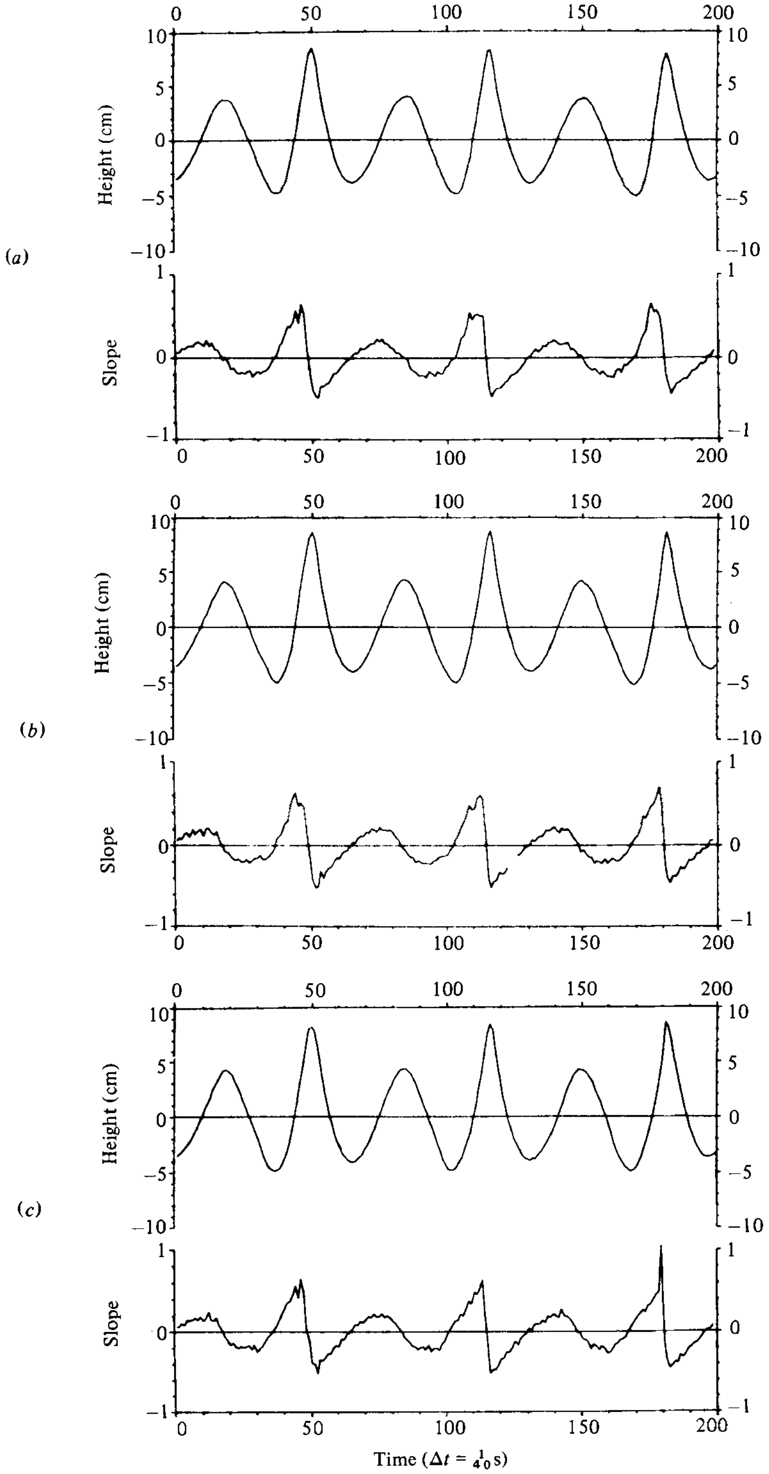

FIGURE 20. For caption see p. 99.

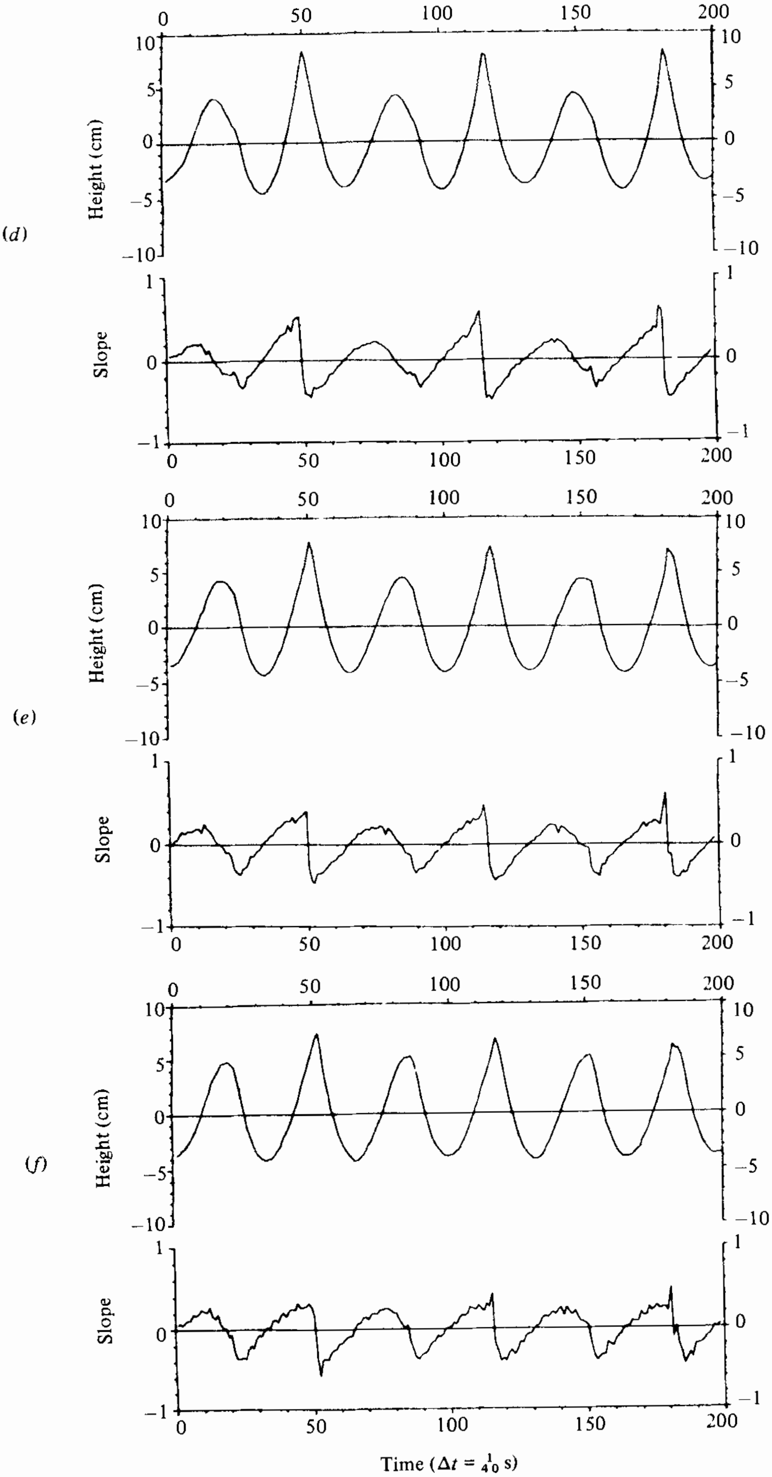

FIGURE 20. For caption see facing page.

(g)

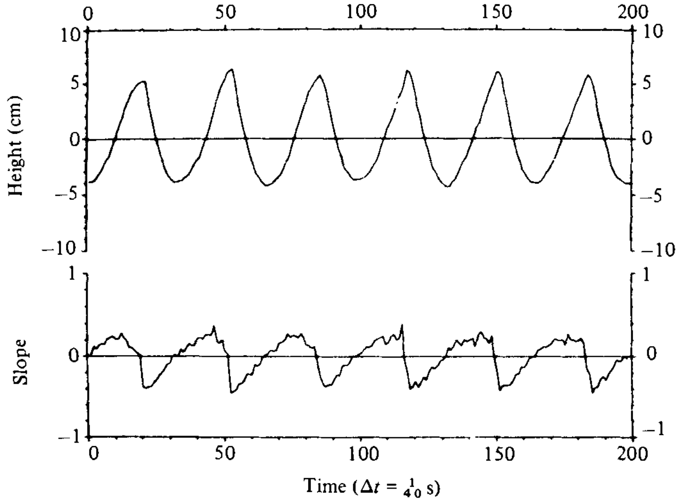

FIGURE 20. Plots of corresponding surface displacement and surface slope for each y in figure 19(*a*).

to those of the Stokes waves existed there, we should have observed them in the wake behind the trailing edge. No such reflected waves are visible in figure 6(*c*). Thus the standing waves cannot be used for explaining our observations. The second explanation is the permanent wave groups obtained analytically by Hui & Hamilton (1979) from the three-dimensional nonlinear Schrödinger equation which is derivable from a further approximation of Zakharov equation (Zakharov 1968). These predicted permanent wave groups have propagation directions either greater or less than a characteristic direction $\Psi_c = \arctan\sqrt{\frac{1}{2}} = 35{\cdot}5°$ away from the fundamental (carrier) wave direction. However, the group-velocity component normal to the Ψ_c direction of the permanent wave groups is equal to the group velocity of the Stokes waves, and is about twenty times larger than the pattern velocity of the observed skew wave patterns for $\Psi = 18{\cdot}5°$. Because of this large discrepancy between the two velocities, the theoretical permanent wave groups found by Hui & Hamilton are not the same as those found in our experimental observation. Perhaps the compelling reason for rejecting the above two interpretations is that the observed skew waves only occur clearly in a very selective narrow steepness range $0{\cdot}16 < a_0 k_0 < 0{\cdot}18$.

Next, we shall try to compare the experimental results with the theoretical computation of steady skew wave patterns appearing as bifurcations from the uniform Stokes waves based on the Zakharov equation (Saffman & Yuen 1980; Meiron *et al.* 1982). It should be stressed that these computations are only approximately correct for moderate and steep waves owing to the assumption of weak nonlinearity underlying the derivation of the Zakharov equation. Generally, these computations overpredict the wave steepness for any given characteristics, as compared with those obtained from the exact water-wave equation (Crawford *et al.* 1981). Consequently one can only hope for qualitative, rather than quantitative, agreement.

Three examples of the free surface corresponding to the bifurcated skew waves for $p = \lambda_0/\lambda_{sx} = 0{\cdot}1$, $q = \lambda_0/\lambda_{sy} = 0{\cdot}4$, and $b_1 = 0$, $0{\cdot}2$ and $0{\cdot}4$ are given by Saffman & Yuen (1980). The example with $b_1 = 0$ corresponds to regular uniform Stokes waves, while the latter two examples correspond to bifurcated skew waves of increasing

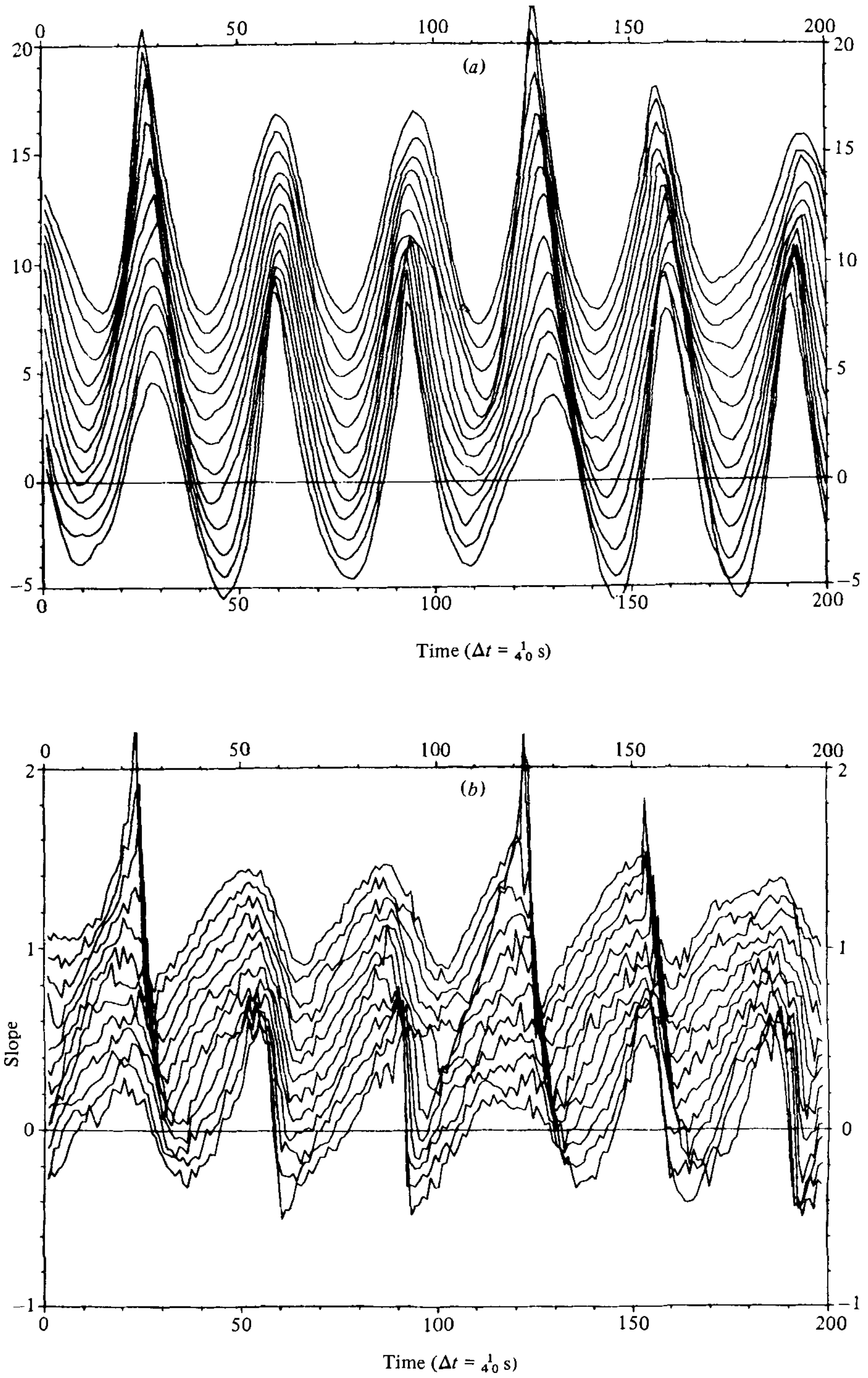

FIGURE 21. (*a*) Plots of wave profiles for L_3 configuration of symmetric waves in the same format as figure 18(*a*). (*b*) Plots of surface slopes corresponding to (*a*).

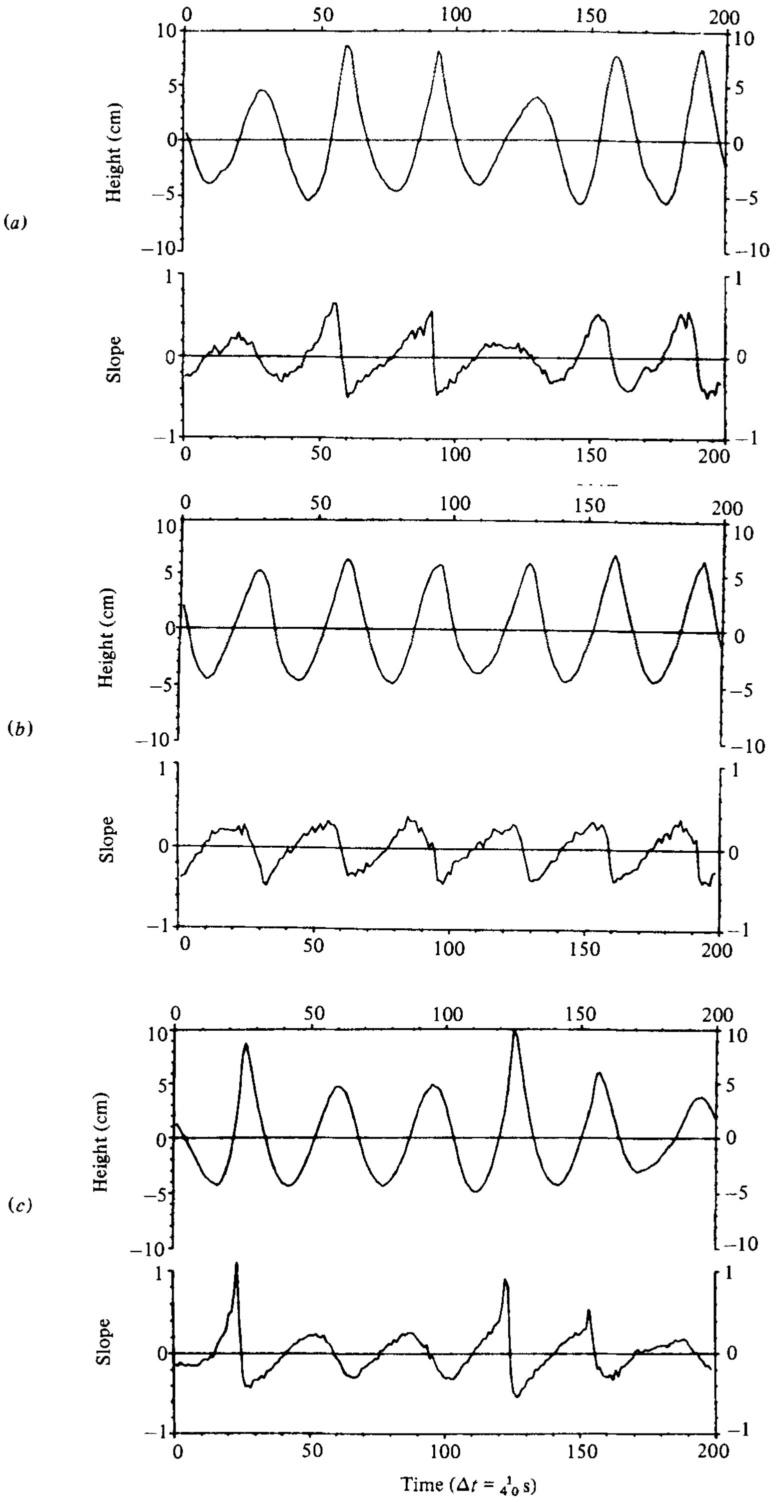

FIGURE 22. Plots of corresponding surface displacement and surface slope for (a) $y = 0$, (b) $\frac{1}{4}\lambda_{BC}$, (c) $\frac{1}{2}\lambda_{BC}$.

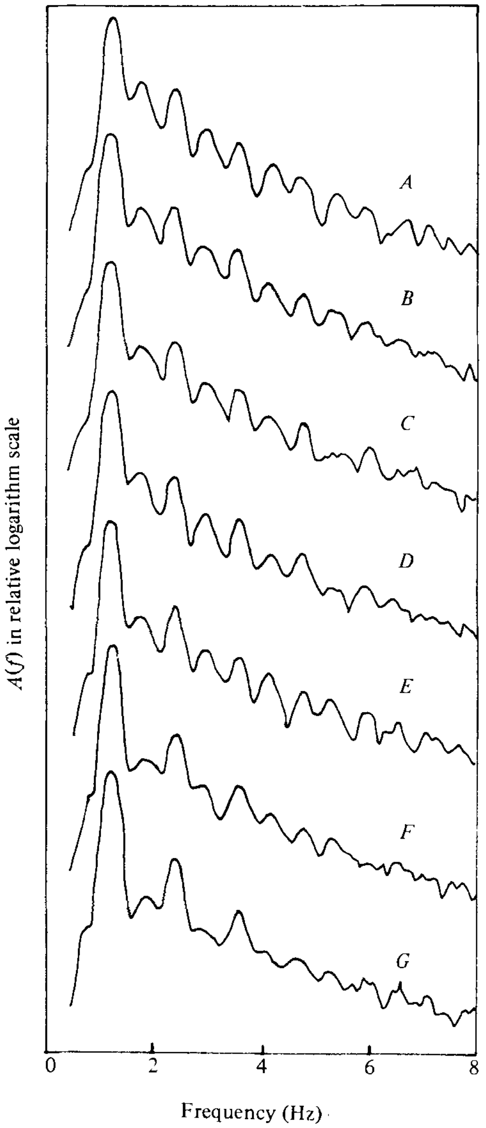

FIGURE 23. Amplitude spectra $A(f)$, which are the amplitudes of the Fourier transforms of wave-surface elevations corresponding to figure 19(a).

degree of bifurcation. The propagation direction Ψ (which is equal to 90° minus the direction of modulation used by Saffman, Yuen and Meiron) for these cases is

$$\Psi = \arctan\frac{p}{q} = \arctan\frac{0\cdot 1}{0\cdot 4} = 14^\circ.$$

The free surfaces resemble the skew wave patterns shown in figures 3 and 6. Further, a critical wave steepness for the bifurcation for these examples (from figure 1 of Saffman & Yuen 1980) is 0·20. This steepness is close to (but slightly larger than) the range of steepness $0\cdot 16 \lesssim a_0k_0 \lesssim 0\cdot 18$ found to be most favourable for occurrence of the phenomenon.

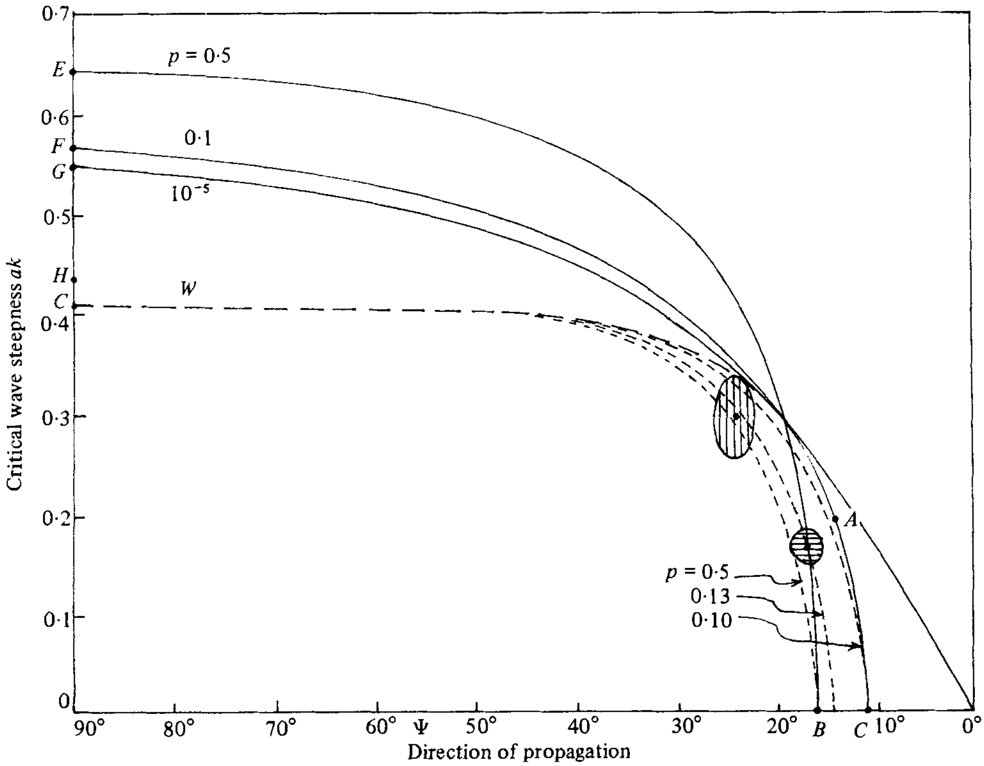

FIGURE 24. Critical bifurcation-wave steepness as a function of propagation angle Ψ; solid lines from Saffman & Yuen (1980), based on Zakharov's equation; the curve marked W (long dashed line) represents the neutral stability curve obtained from Whitham's theory, which is exact for p, q approaching zero; short dashed lines show the expected 'correct' theoretical prediction (see §5 for explanations); horizontally shaded area shows the region of experimental data for the skew wave patterns; the vertically shaded area shows the region of experimental data for the symmetric wave patterns.

We could improve the comparison by understanding a little better the computations by Saffman, Yuen and Meiron. For this purpose, we have reproduced figure 2 of Saffman & Yuen (1980) in our figure 24, which gives the critical bifurcation-wave steepness as a function of propagation direction Ψ. Note that point A marked in figure 24 corresponds to the example cited above. Also plotted in figure 24 are two shaded regions where the skew waves and symmetric waves have been predominantly observed in the experiments. For the skew waves:

$$15^\circ < \Psi < 20^\circ, \quad 0{\cdot}16 < ak < 0{\cdot}18, \quad 0{\cdot}12 < p < 0{\cdot}14, \quad 0{\cdot}3 < q < 0{\cdot}5.$$

For the symmetric waves:

$$23^\circ < \Psi < 27^\circ, \quad 0{\cdot}25 < ak \leqslant 0{\cdot}33, \quad p = 0{\cdot}5, \quad 1{\cdot}1 < q < 1{\cdot}2.$$

Figure 24 indicates that the critical bifurcation-wave steepness for $p = 0{\cdot}5$, $0{\cdot}1$ and 10^{-5} are all over-predicted for large ak; the values of steepness for $\Psi = 90^\circ$ (i.e. $q = 0$) as shown by points E, F and G are well above the Stokes limiting steepness 0·443 (point H). On the other hand, the entire curve for $p = 0$ based on Whitham's theory (Peregrine & Thomas 1979), and the two points B and C for $q = 0$ based on the exact water-wave equation (McLean *et al.* 1980) are theoretically accurate. If we use as the necessary constraints the above known correct limiting points, and the general features of the curves by Saffman, Yuen and Meiron for the critical bifurcation steepness, we might expect the *correct* curves for the critical bifurcation wave steepness based on the exact water-wave equation for $p = 0{\cdot}5$, $0{\cdot}13$ and $0{\cdot}10$ to resemble the dashed lines sketched in figure 24. These *correct* theoretical predictions then agree quantitatively with our experimental observations for both bifurcated skew waves and symmetric waves, as far as the critical wave steepness and the propagation direction are concerned.

The Saffman–Yuen–Meiron theory has built in it an assumption that the component of the phase velocity of the steady skew wave in the fundamental wave direction is the same as that of Stokes waves. In other words, these skew waves are phase-locked to the Stokes waves. On the other hand, the observed skew wave patterns show only a small, yet finite, forward movement relative to the wavemaker at about one-fiftieth of the phase speed of Stokes waves. This discrepancy between the experimental observations and the Saffman–Yuen–Meiron model indicates that the observed skew waves are also not those calculated by these latter authors.

Next, we consider the stability of the skew waves to infinitesimal perturbations, as demonstrated theoretically by Saffman, Yuen and Meiron. What they have shown is that there is no change of stability with respect to infinitesimal disturbances near the bifurcation point. Since the Stokes waves are known to be unstable to subharmonic side-band instabilities of Benjamin–Feir type, the bifurcated skew waves should be subject to the same instabilities, as demonstrated clearly in our experiments. In order to demonstrate the relative stability of the bifurcated skew waves to superharmonic finite disturbances, we conducted some experiments purposely during windy conditions when there are natural wind-generated short gravity waves ($\lambda_0 < 0{\cdot}30$ m) in the basin. Into these pre-existent perturbations, we generated the mechanical waves with $a_0 k = 0{\cdot}17$ and $\lambda_0 = 1$ m. We observed the skew wave patterns as shown in figure 25.

The bifurcation theory (Saffman–Yuen–Meiron) for the skew waves (similarly for symmetric wave does not provide information on the selection rules for the preferred values of p and q, which determine the spatial scales λ_{sx} and λ_{sy} of the skew wave pattern. The example in Saffman & Yuen (1980, figure 4) for $p = 0{\cdot}1$ and $q = 0{\cdot}4$ cited earlier has been chosen based on some earlier experimental observations provided by our earlier investigation. Such selection rules may be related to the three-dimensional instability discovered theoretically by McLean *et al.* (1980), using a linear perturbation analysis of the exact water-wave equation. According to this theory the most unstable mode occurs at $p = 0{\cdot}5$ and $q \simeq 1{\cdot}6$ for $0{\cdot}1 < a_0 k_0 < 0{\cdot}2$. The corresponding propagation direction of this mode is

$$\Psi_m = \arctan\frac{0{\cdot}5}{1{\cdot}6} = 17{\cdot}4^\circ,$$

which is close to the preferred propagation direction of the skew wave patterns,

$$\Psi_s = \arctan\tfrac{1}{3} = 18{\cdot}5^\circ.$$

Figure 24 shows that the theoretical propagation direction of the skew waves is centred around $18{\cdot}5^\circ$ and is relatively insensitive to variation of wave steepness in

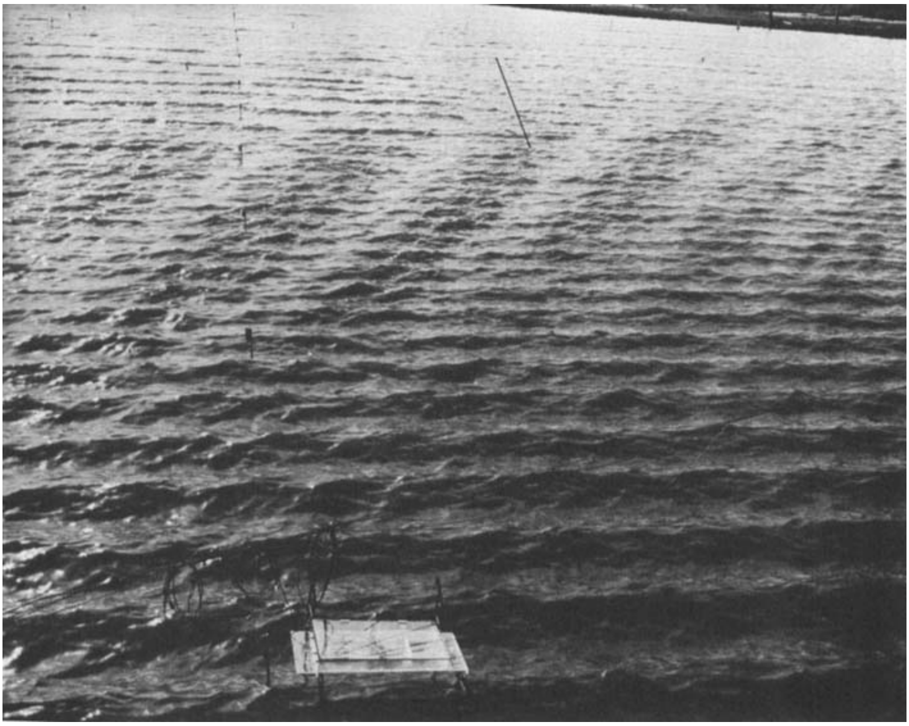

FIGURE 25. Skew wave patterns ($a_0k_0 = 0{\cdot}17$, $\lambda_0 = 1$ m) observed on a background of natural wind-generated short gravity waves with $\lambda_w < 0{\cdot}30$ m in the basin during a windy condition.

the range $0{\cdot}1 < ak < 0{\cdot}20$. The three-dimensional unstable mode has a normal component of phase velocity equal to the Stokes waves. However, the crestwise wavelength of this unstable mode is only about one quarter ($\simeq 0{\cdot}4/1{\cdot}6 = \frac{1}{4}$) of the observed skew waves. Because of this discrepancy, we feel that the observed skew waves could not be explained satisfactorily by the above-mentioned theories.

It is interesting to consider possible effects of the finite crest length of the wavemaker employed in the experiments on the three-dimensional wave patterns. If we had had an infinitely long wavemaker to generate a true two-dimensional Stokes wave with $0{\cdot}16 \gtrsim a_0k_0 \gtrsim 0{\cdot}18$, then we would *not* be able to observe the predominantly '*pure*' skew waves, nor Benjamin–Feir modulations of Stokes waves. Only the diamond-shaped wave patterns due to interactions of the two sets of skew wave patterns and Benjamin–Feir modulations would be observed. Some synthetic aperture radar (SAR) images of hurricane waves seem to indicate existence of such wave patterns in the real oceans (King & Shemdin 1978).

The three-dimensional short-crested symmetric waves observed in the tow tank and the wide basin bear remarkably close resemblance to those spilling breaking waves commonly observed in the growing seas. Some particularly clear pictures of this type of waves in the open ocean can be found in Kinsman (1965, p. 536); there is some regularity in the entire wave pattern, in which several waves are breaking, and the crests of these breakers appear as crescents. Two other photographs (Cokelet 1977, figure 7; Gross 1977, p. 202) show similar features, with more details of waveforms at the breaking points and with some trailing foam behind breaking. Donelan, Longuet-Higgins & Turner (1972) reported some qualitative observations of white-capping in which they noticed that the time interval between successive white caps was roughly twice the wave period. They explained this periodicity as a result of wave groupiness in the growth stage of wind waves.

McLean *et al.* (1980) pointed out that two main types of instabilities exist for waves in deep-water which they called type I and type II. The type I instability is an extension of the well-known side-band instability first discovered by Benjamin & Feir (1967) in the two-dimensional case for small wave steepness and long-wave perturbations. It is predominantly two-dimensional, in that the maximum instability occurs for a two-dimensional perturbation. The type II instability, in contrast, is predominantly three-dimensional, in that maximum instability always occurs for fully three-dimensional perturbations. For small ak, the type I instability dominates. At $ak \simeq 0{\cdot}3$, the type II overtakes type I. The type I instability disappears at $ak \simeq 0{\cdot}39$, while the type II instability continues to increase in magnitude. At $ak \simeq 0{\cdot}4$, the type II instability develops a two-dimensional special case (see McLean *et al.* 1980, figure 1*g*), which is the 'new instability' found by Longuet-Higgins (1978) in his two-dimensional calculations. It should be noted that, even at this point, the maximum growth rate still occurs for fully three-dimensional perturbations.

Another important difference between the type I and II instabilities may help to distinguish them. The perturbation frequency of the type I is not small. The modulational envelope due to the subharmonic instabilities travels with the group velocity, which is roughly half the phase velocity. Hence each wave group displays about twice as many waves in a temporal record as in a spatial record (such as recorded on a photograph). In the type II instability, the perturbation frequency is small in both the two-dimensional case (Longuet-Higgins 1978) and the three-dimensional case (McLean 1982; McLean *et al.* 1980). Hence each wave group in the type II instability travels with the basic phase velocity, and their variation in space looks roughly the same as their variation in a time record. So when in a time record we see alternately high and low crests, it is probably a type II instability. But if we see wave groups with four or more waves, it is probably a type I instability. Thus, it seems to be of no doubt that the three-dimensional type II instability causes the L_2 configuration of symmetric waves.

The above discussion on the linear analysis of instabilities provides only a possible cause for onset of the three-dimensional symmetric waves. Meiron *et al.* (1982) will provide theoretical computations based on a set of approximate equations valid for weak nonlinearity of three-dimensional symmetric wave patterns which are obtained as bifurcations from two-dimensional Stokes waves. These theoretical wave patterns are found to agree well, qualitatively, with the experimental measurements.

6. Conclusions

Based on experimental observations, measurements and comparisons with the existing theoretical computations on the bifurcation and instability of a uniform Stokes wavetrain into the skew and symmetric wave patterns, we may draw the following conclusions.

A uniform (two-dimensional) Stokes wavetrain bifurcates into three-dimensional steady skew wave patterns. The range of wave steepness for the bifurcation is

$0{\cdot}16 < a_0k_0 < 0{\cdot}18$, and the corresponding direction of propagation is from 15° to 20° away from the initial direction of the Stokes waves.

The skew waves are unstable to subharmonic instabilities just like Stokes waves, and are relatively stable to superharmonic perturbations. The growth rate of the bifurcation is of the same order of magnitude as the side-band instabilities for the above steepness range. Three-dimensional compact wave packets form owing to the subharmonic instabilities of the skew wave patterns.

Interactions of the skew wave patterns propagating from different directions also create compact three-dimensional wave packets. The skew waves emerge seemingly without change from the interactions. Thus, in many respects, the skew bifurcated waves behave in the same manner as Stokes waves.

The close overall similarity of the observed symmetric wave patterns to the theoretical computations of steady symmetry wave patterns suggests that these waves can be considered to be bifurcations from an initial steep two-dimensional Stokes wavetrain. The crescent-shaped symmetric waves in the laboratory resemble spilling breakers commonly observed in the ocean, and are self-similar in structure, and relatively independent of initial wave steepness for $0{\cdot}25 < a_0k_0 < 0{\cdot}33$.

The cross-sectional measurements of surface elevation of these symmetric waves reveal three main configurations, with subharmonic periodicity of two, three and four basic wavelengths. The estimated probability of occurrence for these configurations is about 90, 10 and 1 % respectively. The maximum local surface slope on the forward face of the short-crested breakers is much higher than the Stokes limiting slope of 0·577 by as much as 70 % owing to the three-dimensionality of the symmetric waves.

I would like to express my thanks to M. Bergin, P. Marler and R. Myrick for assistance in experiments and data processing, and to Drs A. W. Green and R. Zalkan, and Professors W. H. Hui and M. S. Longuet-Higgins for helpful comments and suggestions that improved an earlier manuscript. I am grateful to Professor P. G. Saffman and Dr H. Yuen for extensive discussions on the results presented herein.

REFERENCES

Benjamin, T. B. & Feir, J. E. 1967 The disintegration of wave trains on deep water. Part 1. Theory. *J. Fluid Mech.* **27**, 417–430.

Cokelet, E. D. 1977 Breaking waves. *Nature* **267**, 769–774.

Crawford, P. R., Lake, B. M., Saffman, P. G. & Yuen, H. C. 1981 Stability of weakly nonlinear deep-water waves in two and three dimensions. *J. Fluid Mech.* **105**, 177–191.

Donelan, M., Longuet-Higgins, M. S. & Turner, J. S. 1972 Periodicity in white caps. *Nature* **239**, 449–450.

Gross, M. G. 1977 *Oceanography – A View of the Earth.* Prentice-Hall.

Hui, W. H. & Hamilton, J. 1979 Exact solutions of a three-dimensional nonlinear Schrödinger equation applied to gravity waves. *J. Fluid Mech.* **93**, 117–133.

King, P. G. & Shemdin, O. H. 1978 Radar observations of hurricane wave directions. In *Proc. 16th Coast Engng Conf.*

Kinsman, B. 1965 *Wind Waves.* Prentice-Hall.

Longuet-Higgins, M. S. 1976 On the nonlinear transfer of energy in the peak of a gravity-wave spectrum: a simplified model. *Proc. R. Soc. Lond.* A **347**, 331–328.

Longuet-Higgins, M. S. 1978 The instabilities of gravity waves of finite amplitude in deep water. II. Subharmonics. *Proc. R. Soc. Lond.* A **360**, 489–505.

McLean, J. W. 1982 Instabilities of finite-amplitude water waves. *J. Fluid Mech.* **114**, 315–330.

McLean, J. W., Ma, Y. C., Martin, D. U., Saffman, P. G. & Yuen, H. C. 1981 A new type of three-dimensional instability of finite-amplitude waves. *Phys. Rev. Lett.* **46**, 817–820.

Meiron, D. I., Saffman, P. G. & Yuen, H. C. 1982 Calculation of steady three-dimensional deep-water waves. *J. Fluid Mech.* **124**, 109–121.

Peregrine, D. H. & Thomas, G. P. 1979 Finite amplitude deep water wave on currents. *Phil. Trans. R. Soc. Lond.* A **292**, 371–390.

Saffman, P. G. 1981 Long wavelength bifurcation of gravity waves on deep water. *J. Fluid Mech.* **101**, 567–581.

Saffman, P. G. & Yuen, H. C. 1980 A new type of three-dimensional deep-water waves of permanent form. *J. Fluid Mech.* **101**, 797–808.

Su, M.-Y., 1981 Long-time evolution of deep-water surface wave trains of moderate steepness (unpublished manuscript).

Su, M.-Y., Bergin, M., Marler, P. & Myrick, R. 1982 Experiments on nonlinear instabilities and evolution of steep gravity-wave trains. *J. Fluid Mech.* **124**, 45–72.

Zakharov, V. E. 1968 Stability of periodic waves of finite amplitude on the surface of a deep fluid. *J. Appl. Mech. Tech. Phys.* **2**, 190–194.